Contents lists available at ScienceDirect

LITHOS

Petrology of the magmatic system beneath Osorno volcano (Central Southern Volcanic Zone, Chile)

Tonin Bechon [a,*], Melvyn Billon [a], Olivier Namur [b], Olivier Bolle [a], Paul Fugmann [a], Hélène Foucart [a,c], Jean-Luc Devidal [d], Nicolas Delmelle [a], Jacqueline Vander Auwera [a]

[a] *Liège University, Laboratoire de pétrologie, Université de Liège (B20), Allée du Six Août, 12, Liège 4000, Province de Liège, Belgium*
[b] *Leuven University, Geology, Leuven (Arenberg), Katholieke Universiteit Leuven, Celestijnenlaan 200e - box 2408, Leuven 3001, Vlaams-Brabant, Belgium*
[c] *Institut Scientifique de Service Publique, Rue du Chéra 200, Liège 4000, Province de Liège, Belgium*
[d] *Laboratoire Magmas et Volcans, Université Clermont Auvergne - CNRS - IRD, OPGC 6, avenue Blaise Pascal, campus universitaire des Cézeaux, Aubière 63178, Région Auvergne-Rhone-Alpes, France*

ARTICLE INFO

ABSTRACT

Petrological studies of volcanic systems and magmatic processes provide small-scale information that are inaccessible to the current resolution of geophysical tools. In the Southern Volcanic Zone of the Chilean arc, Osorno ranks sixth in the official risk classification in a region of increasing vulnerability due to soaring human activities coupled with lahar hazard and the threat of a tsunami induced by a flank collapse. However, its magmatic system remained poorly investigated. Here, we present and integrate to existing geophysical models a comprehensive set of petrographic and geochemical data including whole-rock and mineral major and trace element analyses, associated with detailed numerical modelling to constrain the storage conditions below Osorno. To capture the full complexity of the system, over 154 samples of all known major units of the volcano have been collected. They cover a large range from tholeiitic primary basalt (Mg# = 0.72 and $\geq$ 50 wt% SiO$_2$) to rhyodacite (Mg# = 0.18 and $\geq$ 70 wt% SiO2), displaying a compositional gap within andesite (59–63 wt% SiO$_2$). This gap results either from andesitic melt thermal instability or from the interstitial melt extraction of the crystal mush. Basalt and basaltic andesite lava with plagioclase and olivine ($\pm$ clinopyroxene) are dominant. Their crystallinity largely varies from 1 to 53 area % with the lowest values in the most evolved basaltic andesites. Dacites are limited to three small domes with low crystallinities between 7 and 13 area %. The presence of diktytaxitic enclaves within the dacites indicate minor mingling with a less differentiated melt. Water-bearing phases are generally absent, except for one dacite sample where few small amphibole crystals occur. Petrology, chemical data and thermobarometric results imply shallow fractional crystallization of troctolitic, gabbroic and gabbronoritic cumulates. Differentiation dominantly takes place between 2 and 3 kbar (6–10 km) and results from a water-poor ($\approx$1 wt% H$_2$O), tholeiitic parental melt. No evidence of high-pressure fractionation was observed. We interpret this differentiation depth as Osorno's main storage zone. It correlates with the depth of the intracrustal discontinuity and seismic reports below the volcano. Only the upper half of the storage zone, imaged with geophysical methods, was erupting. We suggest a comparable behavior for a potential future event.

1. Introduction

Osorno is an active stratovolcano of the Southern Andes that has a history of effusive and explosive eruptions (Petit-Breuilh, 1999, Volcanic Explosivity Index (VEI) = 1 to 3) with a last major volcanic event dated at January–December 1835. Moreover, the ice capped summit of its perfectly shaped cone has the potential to produce lahars if in contact with eruptive products, thus threatening the surrounding communities in a region that is rapidly growing economically, partly owing to increased tourism. Osorno is sixth on the Chilean volcanic risk ranking (Contreras Vargas et al., 2020). Available data indicate significant differences between Osorno and its neighboring volcano, Calbuco, that is only 26 km away. At Calbuco, the explosivity is higher, as witnessed by its 2015 sub-Plinian eruption, andesites are much more abundant and amphibole is common whereas it is reported to be notably absent at Osorno (Lopez-Escobar et al., 1992; Moreno Roa et al., 2010). These

differences likely reflect variable H_2O content in the parent magma of both volcanoes as suggested by petrological data: 3.0–3.5 wt% H_2O and 3.5–4.5 wt% H_2O were respectively estimated by chemical modelling for the Calbuco basalts (Vander Auwera et al., 2021) and basaltic andesites (Namur et al., 2020) whereas Morgado (2019), using r-MELTS algorithm, estimated 1.5 wt% H_2O in the basaltic andesite of the Osorno 1835 eruption. However, the parameters that control such differences between two volcanoes that are so closely related have not yet been successfully constrained (as discussed by Vander Auwera et al., 2021) partly because detailed petrological and geochemical data are still

missing for Osorno. Previous studies used a very limited number of samples (Klerkx, 1964; Lopez-Escobar et al., 1992; Tagiri et al., 1993) or were focused on one specific event (Morgado, 2019, the 1835 eruption). Here, we provide a comprehensive petrological study of Osorno in order to constrain the parent magma composition, including the melt H_2O content, the dominant magmatic processes as well as the depth of the main storage region which will be compared with the recent density and magnetotelluric models from Tassara and Echaurren (2012) and Díaz et al. (2020).
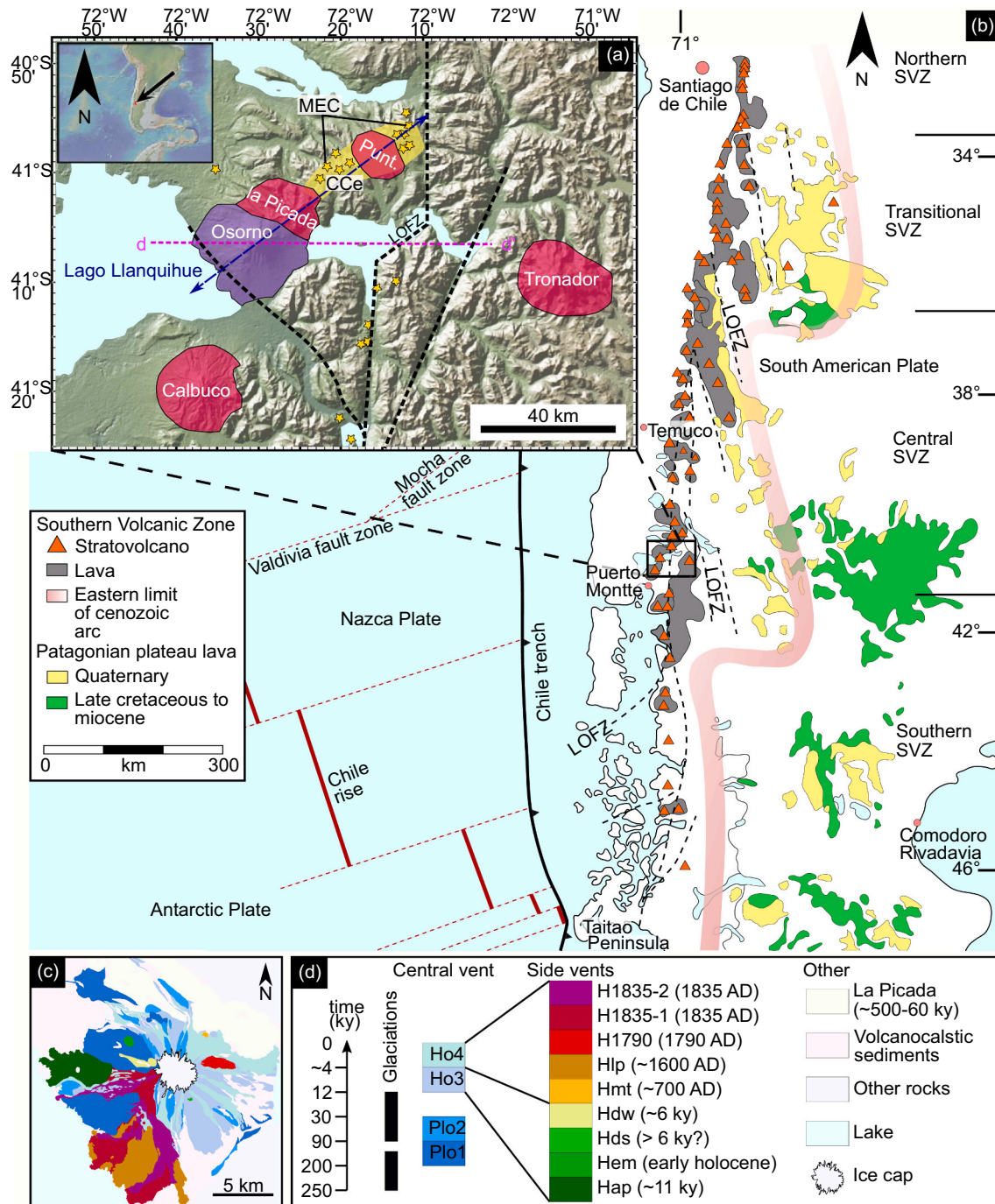

Fig. 1. Geological setting of the Osorno volcano. (a) and (b) surroundings (Ryan et al., 2009, modified) and regional (Stern et al., 2007, modified) maps respectively (Punt. = Puntiagudo; CCe = Cordon Cenizos; MEC = Minor Eruptive Centers; LOFZ = Liquiñe-Ofqui Fault Zone; SVZ = Southern Volcanic Zone); (c) and (d) simplified geological map and stratigraphic log from Osorno after Moreno Roa et al. (2010). Inset in (a) shows the location in Southern America. For sampling map, see.kmz file in supplements.

2. Geology

The Andean arc results from the subduction of the Cocos, Nazca and Antarctica oceanic plates below the South American continental plate. It has been subdivided into four different sections (Northern: 10°N-5°S, Central: 15–27°S, Southern: 33.3–46°S and Austral: 49–55°S Volcanic Zones) separated by volcanic gaps due to flat slab segments (Stern et al., 2007). The Southern Volcanic Zone (SVZ) (Fig. 1) is further subdivided into four sub-zones: Northern (NSVZ: 33.3–34.4°S), Transitional (TSVZ: 34.4–38°S), Central (CSVZ: 38–42°S) and Southern (SSVZ: 42–46°S) (Hickey-Vargas et al., 2016b; Stern et al., 2007). The NSVZ is characterized by a relatively thick continental crust (50 km) and lavas are predominantly andesitic or dacitic in composition. Hydrous minerals such as amphibole or biotite are common (Hickey-Vargas et al., 2016b; Lopez-Escobar et al., 1995; Stern et al., 2007). In the TSVZ, basaltic andesites dominate and basalts are rare (Hickey-Vargas et al., 2016b). Both sections are likely affected by crustal contamination (Hildreth and Moorbath, 1988; Stern et al., 2007). The continental crust underlying the CSVZ and SSVZ (Fig. 1) volcanoes thins from north (≈40 km) to south (30 km) and volcanic centers erupt dominantly basalts and basaltic andesites. These two segments are cut by the LOFZ, a major transpressive transcrustal fault system that facilitates magma ascent (Cembrano and Lara, 2009; Hickey-Vargas et al., 2016b). Volcanoes (stratovolcanoes and minor eruptive centers) are aligned along the main LOFZ segments (N10°E), on NE-SW tension gash segments flanking the LOFZ and on a NW-SE segment following a pre-Andean fracture (Cembrano and Lara, 2009). The evolution of their magmas along the liquid lines of descent is likely dominated by a process of fractional crystallization (Thorpe et al., 1984). Although inaccurate (Schindlbeck et al., 2014), the main reported difference between the SSVZ and the CSVZ is the lack of hydrous phases in the silicic products of the CSVZ (Stern et al., 2007).

Osorno is a recent and active Holocene-Pleistocene stratovolcano (≤200 ky) in the CSVZ. It is built on Mesozoic to Cenozoic plutonic basement, as well as on lavas and volcanoclastic sediments from the Pleistocene volcano La Picada (e.g., Adriasola et al., 2006; Moreno Roa et al., 2010). Historical descriptions of volcanic activities (1719 to present) were compiled by Petit-Breuilh (1999). Osorno is part of a NE trending volcanic chain including the Cordon Cenizos fissural vent, the La Picada and Puntiagudo stratovolcanoes and several recent minor eruptive centers (MECs) mostly located on the Cordon Cenizos fissural vent (Fig. 1). This volcanic chain is built along a secondary NE-SW fault which is oblique to the LOFZ (N10°E) (Cembrano and Lara, 2009; Díaz et al., 2020; Lopez-Escobar et al., 1995; Moreno Roa et al., 1979) and Osorno is additionally located on another secondary fault trending N50–60°W (Díaz et al., 2020; Moreno Roa et al., 2010). Moreno Roa et al. (1979) presented the first study of the Osorno-Puntiagudo volcanic chain and gave the relative order of appearance for each volcano: Cordon Cenizos and La Picada were built first during the late Pliocene, followed by Osorno and Puntiagudo during the glacial Pleistocene; the MECs were created during late glacial Pleistocene.

The last major volcanic activity of Osorno (VEI 3) occurred in 1834–1835 (Petit-Breuilh, 1999). This violent strombolian eruption at the main crater was associated with lava flows and lahars from adjacent/fissural vents. It was followed by a minor strombolian phase in 1837–1838, possibly associated with lava flow(s). Since then, only fumarolic activity and one suspected eruption (1850) have been reported (Petit-Breuilh, 1999). Based on on previous works (Bruhns, 1853; Lopez-Escobar et al., 1992; Moreno Roa et al., 1979; Tagiri et al., 1993) and using geomorphology, relative or absolute dating, Moreno Roa et al. (2010) subdivided central vent eruptive products (lava and pyroclasts) from Osorno in four temporal units (two Pleistocene and two Holocene) to explain the different building stages of the volcano (Fig. 1c, d). Units 1 (Plo1) and 2 (Plo2) respectively occurred during the Santa Maria glaciation or interglacial era (ca.200 ky - 110 ky) and Llanquihue (ca. 90 ky - 12ky) glaciation while units 3 (Ho3) and 4 (Ho4) emplaced after the Llanquihue glaciation and are separated by a series of explosive events (ca. 4 ky). Five flank scoria cones are associated with unit 4 (Hmt, Hlp, H1790, H1835–1, H1835–2) and two flank scoria cones (Hap, Hem) plus two flank domes (Hds, Hdw) are associated with unit 3 (Fig. 1c, d).

According to Bruhns (1853); Klerkx (1964); Lopez-Escobar et al. (1992); Moreno Roa et al. (2010); Tagiri et al. (1993), erupted lavas are dominated by basaltic andesites and basalts, but range in composition from basalt (≥49% SiO_2) to dacite (≤70% SiO_2) with a Daly gap in the andesitic composition (59–63% SiO_2) (Fig. 2). The trend intersects the limit between the calk-alkaline and tholeiitic fields defined by (Irvine and Baragar, 1971) and compositions are very similar to those reported for La Picada lavas (Vander Auwera et al., 2019). The absence of erupted andesitic rocks may be related to rheological factors (critic crystallinity threshold) which impede eruptions of intermediate magmas (Lopez-Escobar et al., 1992; Vander Auwera et al., 2019). Rare rhyodacitic compositions resulting from crystal mush interstitial melt extraction were evidenced at La Picada (Vander Auwera et al., 2019). Eruptive products are composed of olivine, plagioclase, augite, orthopyroxene, apatite, ilmenite and spinel (magnesio-chromite and titanomagnetite). According to Klerkx (1964) olivine and plagioclase crystallize first, followed by clino- and orthopyroxene, the accessory phases being the lasts. Some glass (interstitial and in melt inclusions) and plutonic enclaves are also reported (Bruhns, 1853). Morgado (2019) calculated the pre-eruptive conditions of the 1835 eruption. He obtained a temperature of ≈ 1140°C, with oxygen fugacity (fO_2) equal to QFM + 0.3 (QFM = quartz-fayalite-magnetite equilibrium) and a H_2O melt content of 1.5 wt % at 52.2–52.9 wt% SiO_2. The calculated magma storage depth is 4.5 km. This is consistent with values reported for La Picada by Vander Auwera et al. (2019) (≈ 2 kbar and fO_2 = NNO-0.3 = QFM + 0.3) and with the geophysical model of the magma chamber realized by Díaz et al. (2020) (≈ 4–18 km).

3. Methods

3.1. Sampling

Sampling was completed across several years (2012, 2013, 2014, 2015, 2016, 2019). A set of 154 samples (96 lavas, 38 pyroclastic deposits, twelve loose blocks, one black scoria, one crystal rich enclave, six plutonic rocks from the basement) around Osorno volcano and four samples from minor eruptive centers (MECs) ontop of Cordon Cenizos (two pyroclastic deposits and two lavas) were collected. All units described by (Moreno Roa et al., 2010) were covered. An undescribed dacitic unit underlying the 1790 pyroclastics was also sampled (OS42) and will be assigned to unit Hde (Holocene, domo este) to follow the classification of Moreno Roa et al. (2010). Sampling coordinates are available in Table S1.

3.2. Textural and petrographic analysis

Microscopic observations were made on 123 thin sections. Quantitative mode analysis of plagioclase, olivine, clinopyroxene, orthopyroxene, amphibole, oxides, apatite and diktytaxitic enclaves (+secondary phases) was applied using three different techniques: (1) point counting analysis of 25 samples using a PELCON automatic point counter (n = 1510–4464 points/sample); (2) digital classification of mineral populations on 10 samples using a TUSCEN Michrome 6 camera, the Gimp and the ImageJ software package for manual segmentation and classification (n = 543–9949 crystals/sample); and (3) by chemical mapping of sample OS 136 using a SEM JEOL JSM-6510 with EDX (Bruker-AXS XFlash, silicon drift 153 detector) at the Centre de Recherches Pétrographiques et Géochimiques (CRPG, Nancy, France). The threshold between crystal and matrix was defined at 100 μm. Additional details are available in Appendix A. Supportive back scattered SEM images used for illustration were taken at the Faculty of Georessources and Material Engineering (RWTH) in Aachen (Germany) using a QEMSCAN.
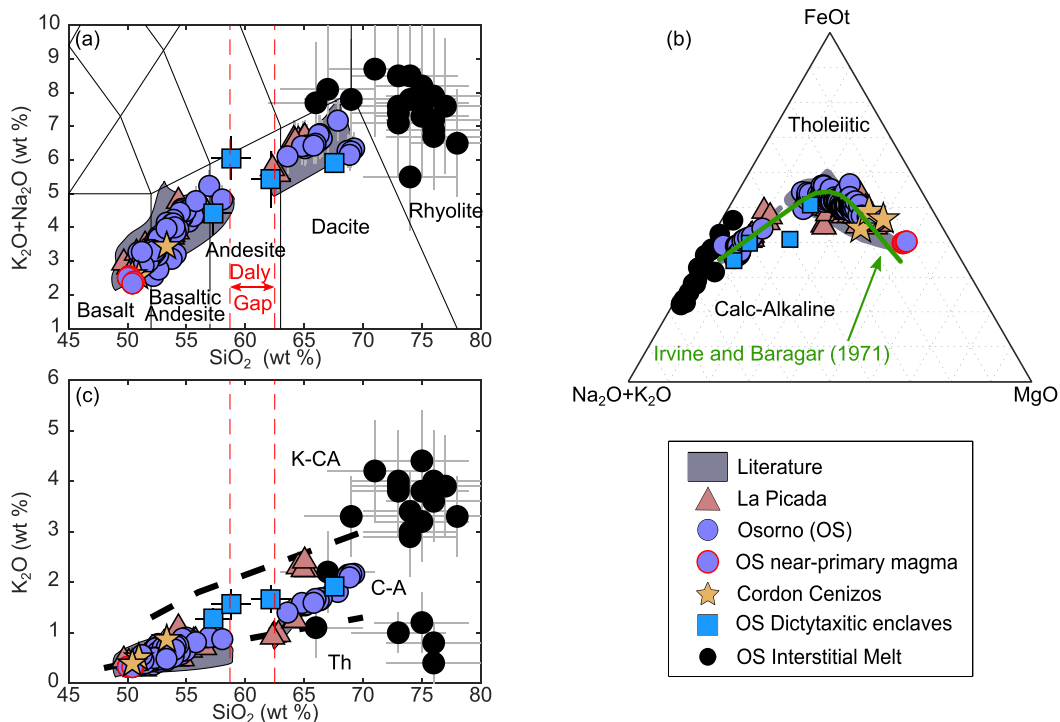
Fig. 2. Selection of classification diagrams. (a) Total Alkali vs. Silica (TAS) diagram. (b) $Na_2O + K_2O$-FeO_t-MgO (AFM) plot with Irvine and Baragar (1971) limit between tholeiitic and calc-alkaline fields. (c) K_2O versus SiO_2 affinity cross-plot after Peccerillo and Taylor (1976); Th = tholeiitic; C-A = calc-alkaline; K-CA = high-K calc-alkaline. Literature data for Osorno (grey fields) are from Deruelle (1982); Jicha et al. (2007); Klerkx (1964); Lopez-Escobar et al. (1992); Moreno Roa et al. (1979, 2010); Tagiri et al. (1993); Wehrmann et al. (2014). La Picada (Vander Auwera et al., 2019) and Cordon Cenizos bulk rock compositions (yellow stars) are also shown for comparison. The limits of the compositional Daly gap are shown by red dashed lines. Error bars represent the 2σ precision. (For interpretation of the references to colour in this figure legend, the reader is referred to the web version of this article.)

3.3. Mineral and glass chemistry

The major element mineral chemistry was measured by electron microprobe at the Laboratoire Magma et Volcans (LMV, Clermont-Fd, France) on a CAMECA SX100 (2018) and a CAMECA SXFIVE Tactis LaB6 (2019). CAMECA SX100 results were obtained with an accelerating voltage of 15 kV, a beam current of 10 nA except for Ni (100 nA) and a focused beam (1 μm). Na and K were measured first to minimize alkali loss. Peak counting times were 20 s for Mg and Mn, 30 s for Fe and Ca, 10 s for Si, Ti, Al, Na and K as well as 60 s for Ni. Glass was measured at 15 kV with a defocused beam size 5 or 10 μm at currents of 4 or 8 nA respectively. Counting times were 40 s for K and Fe, 30 s for Mn, 20 s for Al and Mg and 10 s for other elements. CAMECA SXFIVE Tactis results were obtained using an accelerating voltage of 15 kV, a beam current of 15 nA and a focused beam except for 33 olivine measurements (from samples OS83, CCe1, CCe4) for which the current has been increased to 100 nA to lower the detection limit on Al. Na was measured first to minimize Na-loss. Counting times were 10 s for all the elements excepted for Ni and Al in olivine (20 s and 60 s, respectively). Further calibration details are available in Appendix A. Some olivine and clinopyroxene grains from scoriaceous pyroclastic deposits (H1835–1, H1835–2, H1790, Hmt) were individually mounted in epoxy and analyzed using the same conditions. Their host rock bulk composition were not analyzed due to possible large ash contamination from various Calbuco eruptions nested in the vacuoles. Errors on all measurements are available in Tables S3 to S8.

In-situ trace element analyses ([6]Li, [7]Li, [39]K, [43]Ca, [44]Ca, [49]Ti, [53]Cr, [59]Co, [60]Ni, [85]Rb, [88]Sr, [89]Y, [90]Zr, [93]Nb, [133]Cs, [137]Ba, [139]La, [140]Ce, [141]Pr, [146]Nd, [147]Sm, [153]Eu, [157]Gd, [159]Tb, [163]Dy, [165]Ho, [166]Er, [169]Tm, [172]Yb, [175]Lu, [178]Hf, [181]Ta, [208]Pb, [232]Th, [238]U) were performed on a Thermo-fischer Element XR ICP-MS coupled to Resonetics M-50 excimer Ar/F

laser ablation system operating at a wavelength of 193 nm at LMV. Details on the calibration, accuracy, precision and errors are given in Appendix A and Table S9.

3.4. Bulk rock chemistry

Whole rock major and trace element compositions of 131 samples (all lavas, enclaves, loose blocks, basement samples and only few pyroclasts) were measured by XRF using a X-ray fluorescence Thermofisher PERFORM'X at the University of Liège (Belgium) and by inductively coupled plasma mass spectrometry (ICP-MS) using a Thermo Scientific X-Series 2 ICP-MS with a third generation collision cell at the Musée Royal d'Afrique Centrale (Tervuren, Belgium). Alteration crusts were removed before crushing samples with a hammer on an anvil. The powdering the remaining chips were then powdered in a Fritsch pulverisette planetary mill. Loss on ignition was determined on 1 g of powdered sample heated at 1000 °C for 2 h. Major element analyses were performed on lithium tetra- and meta-borate fused glass discs prepared with 0.35 g of rock powder. For ICP-MS, 200 mg of powder was melted at 1000 °C for 60 min in 1 g of $LiBO_2$ (alkali fusion) in a Pt crucible. Molten samples were then dissolved in 5% HNO_3 and diluted to a volume of 250 ml with distilled water. Samples were further diluted as necessary to decrease the total dissolved solids below 0.2%. Bulk compositions of diktytaxitic enclaves (<5 mm) was determined using modal mineral proportions and chemical compositions. Calibration details, accuracy, precision and diktytaxitic enclave calculations and composition estimates are available in Appendix A.

4. Results

4.1. Bulk rock chemistry

Osorno bulk rock major compositions (Tables S1-S2) broadly overlap with the bulk rock compositions from Cordon Cenizos and La Picada. They range from basalt to dacite (50–70 wt%). A compositional Daly gap in the andesitic field (59–63 wt% SiO_2) splits the trend into two parts. The reconstructed compositions of the diktytaxitic enclaves plot with a rather large uncertainty in the andesitic and dacitic fields. As previously observed by Moreno Roa et al. (2010), a few samples (OS26, OS82, OS83, OS140, OS141), very close in bulk rock composition (major and traces), represent near-primary mantle derived magmas with Mg# = 0.72 (Fe^{2+} calculated using Kress and Carmichael (1991) at NNO-0.3

according to the fO_2 estimates from Morgado (2019); Vander Auwera et al. (2019)), 10.23–10.53 wt% MgO, 584–745 ppm Cr, 171–179 ppm Ni and measured olivine composition up to Fo_{89} in OS83. With increasing SiO_2 content, CaO and MgO decrease respectively from 11 to ≤ 1 wt% and from 10 to ≤ 1 wt%, whereas Na_2O and K_2O respectively increase from 2 to ≈ 6 wt% and ≤ 0.5 to 4.5 wt% (Figs. 2 and 3). The trends of the other oxides (Al_2O_3, Fe_2O_3, MnO, TiO_2, P_2O_5) display a slope change between 52 and 56 wt% SiO_2. Al_2O_3 starts around 16 wt% in near-primary compositions, scatters from 16 wt% to ≈ 21 wt% at 52 wt% SiO_2 and then decreases down to ≤ 11 wt%. Fe_2O_{3t}, P_2O_5, TiO_2, MnO displays a similar behavior with respective start around 9, 0.1, 0.6, 0.15 wt% in near-primary compositions, a maximum at 12, ≈ 0.3, 1.5, ≤ 0.2 wt% around 53, 57, 55, 55 wt% SiO_2 and a decrease down to ≥ 2, ≈ 0.1, ≥ 0.1, ≤ 0.05 wt% (Fig. 3). Crystallization of apatite,
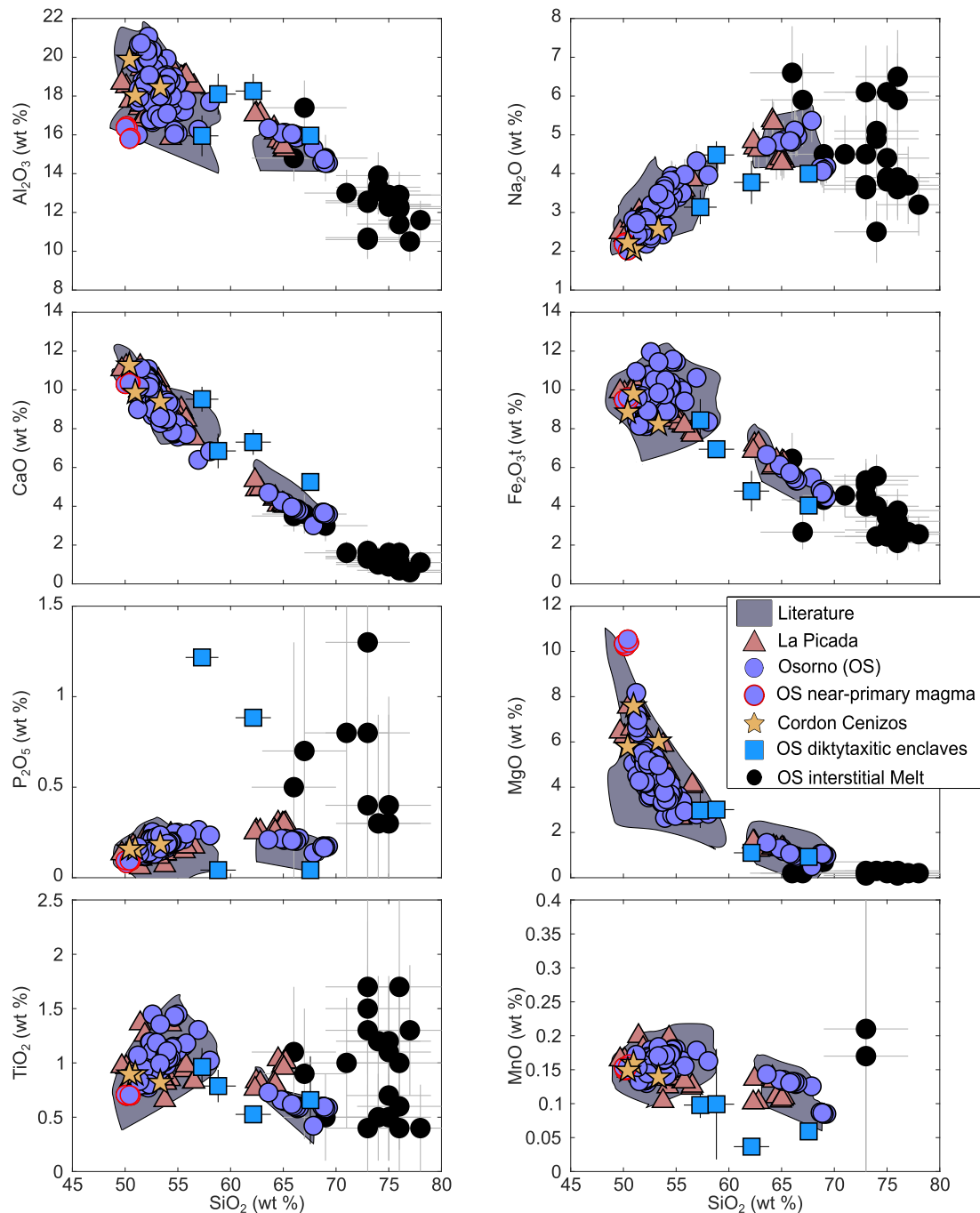

Fig. 3. Harker diagrams of major elements. Values are normalized to 100% on a volatile-free basis with total Fe as Fe_2O_{3t}.

titanomagnetite and plagioclase respectively explain the decrease in P_2O_5, TiO_2 and Fe_2O_{3t}, Al_2O_3. Cr and Ni behave as compatible elements whereas Rb, Ba, Th, Zr, Nb are incompatible (Fig. 4). Trace elements (Fig. 5a) display typical arc setting primitive mantle normalized spider diagrams with a general enrichment from LILE towards HREE, negative anomalies in Nb and Ta, and positive anomalies in Pb, K and Sr. Dacitic lavas generally have higher trace element contents, except for Ti, Eu, Sr. The fractionation between LREE and HREE is moderate in basalts with La/Yb ≤3.3 (Fig. 5b) and increases slightly in dacites (La/Yb ≤5.5). The three Cordon Cenizos samples follow the pattern of the basalts and basaltic andesites, except for Sr that is more enriched than in Osorno's lavas. They also show a higher degree of fractionation between LREE and HREE (La/Yb = 4.22–7.12).

4.2. Textural analysis and mineral compositions

General observations: The overall crystallinity (Appendix B) is low in near-primary basalts (≤8 area %, OS140) but higher in other basalts (12 area % - 53 area %). Textures are phyric for the near-primary magmas and straddle between phyric to glomerophyric for other basalts. Basaltic groundmass is intersertal to hyalopilitic. Basaltic andesites display the most variable textures. Most of them resemble to the basalts, however a sharp change from highly crystalline to aphyric textures is observed in the most evolved ones (from 40 area % to 1 area %). Textures of crystal poor basaltic andesites and the andesite are either pilotaxitic or still glomerophyric with a hyalopilitic groundmass. The same texture is also observed in the dacites in which the crystallinity remains moderate (7 area % - 13 area %). Mg-rich olivine and chromite are the
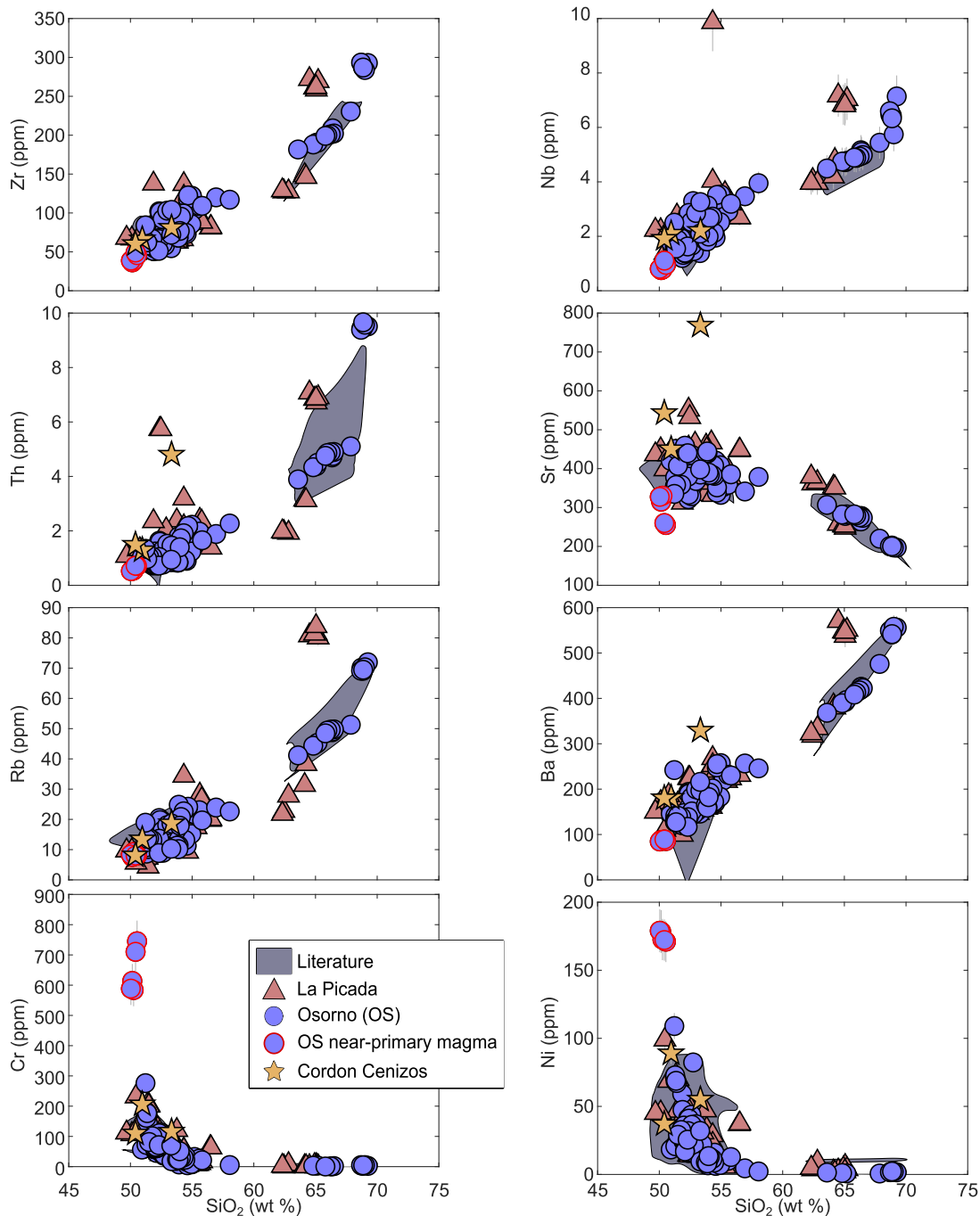

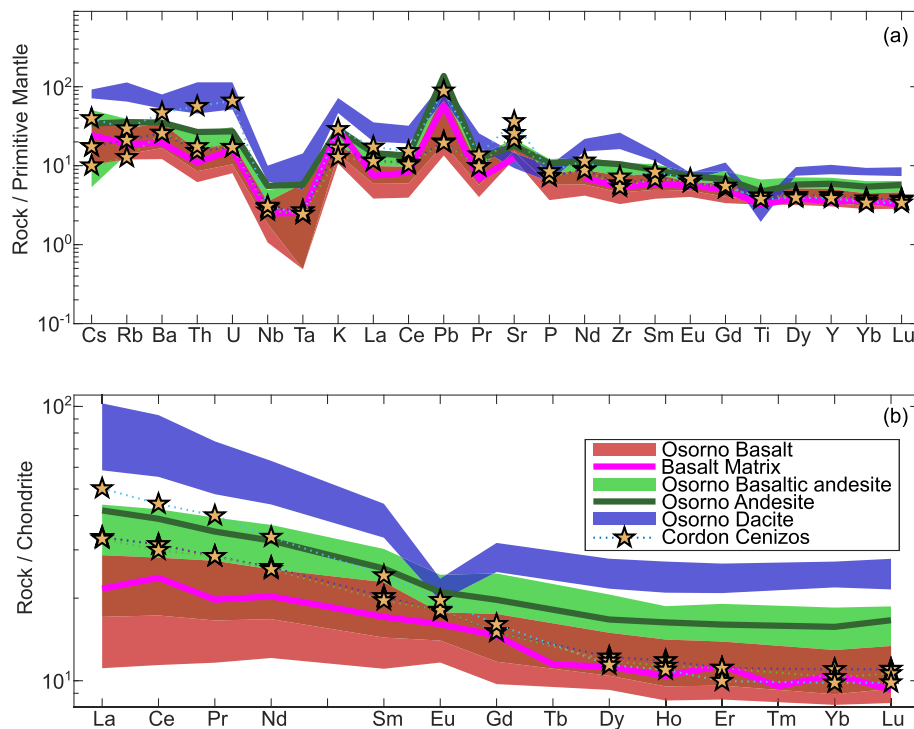Fig. 4. Harker diagrams of selected trace elements.

Fig. 5. Spider diagrams of bulk rock trace elements. (a) Primitive mantle-normalized spider diagrams and (b) REE patterns normalized to C1 chondrite (Sun and McDonough, 1989).

only phenocrysts in near-primary basalts and they are associated with plagiocase, titanomagnetite and occasionally clinopyroxene in other basalts and basaltic andesites. Some evolved basaltic andesites also contain orthopyroxene phenocrysts. The dacite mineralogy is composed of two pyroxenes, plagioclase, titanomagnetite and apatite except in the Hde dome where orthopyroxene is replaced by Fe-rich olivine and in the Hdw dome where traces of brown hornblende were identified for the first time at Osorno. Diktytaxitic enclaves are common in the dacites (Appendix B). In most thin sections, glomerocrysts, used here as a synonym of crystal clots, clusters or aggregates are observed (Appendix C). They are anorthositic, dunitic, wehrlitic, olivine-gabbroic or gabbroic to gabbro-noritic compositions in the basalts and basaltic andesites and compositions in the dacites. In some thin sections (OS21, OS78), glomerocrysts are very abundant whereas phenocrysts are rare. Melt pools were observed in the dacites, usually associated with glomerocrysts. In other rocks, the melt is limited to matrix interstices (few μm only) or inclusions in minerals which are too small to obtain good EMPA analysis. Few reliable (no obvious signs of contamination from surrounding minerals) interstitial rhyodacitic melt analyses extend the bulk rock trend to higher SiO_2 contents (Fig. 3). All EMPA, LA-ICP-MS and phase proportions measurements are available in Tables S3 to S11.

Plagioclase (Pl) is the most abundant phase (0–51 area %) and displays complex textures (Fig. 6), especially in basalts and basaltic andesites. Unzoned and zoned crystals with normal, reverse or patchy zoning are observed. Sieved or partly resorbed textures are also generally present and melt inclusions are common. The An content (molar Ca/(Ca + Na)); Fig. 6a) ranges from An_{92-69} in basalts to An_{92-34} in basaltic andesites with rims being generally more albitic than cores and An_{60-40} in dacites. Plagioclase displays strong Sr and Eu positive anomalies (Fig. 6c) and LREE concentrations are slightly higher in dacite hosted plagioclase.

Olivine (Ol) is less abundant with mode between 0 and 7 area % in basalts, basaltic andesites and in dacitic unit Hde. Crystals are euhedral to sub-euhedral with partially resorbed rims or coronas of pigeonite or orthopyroxene and titanomagnetite. Some grains contain melt or chromite inclusions (Fig. 7d) and can be altered into iddingsite or chrysotile

in a few loose block samples. The Fo content (molar Mg/(Mg + Fe$_t$)) decreases from Fo_{89-62} in basalts to Fo_{82-49} in basaltic andesites (Fig. 7a). The compositions of olivine from the pyroclasts (Fo_{81-70}) overlap with those in the basalts while olivines from Cordon Cenizos (Fo_{85-74}) are compositionally similar to those from the most primitive basalts. Fe-rich olivine (Fo_{29-24}, Fe-Ol), which is an important phase only in the Hde dacitic unit (Fig. 7e), often includes apatite needles or titanomagnetite, and is usually fractured and altered into an orange phase (iddingsite?). Olivine cores are not perfectly in equilibrium (Kd = 0.30 ± 0.03; Putirka (2008)) with their respective host bulk rock compositions (Fig. 7a). Olivine is depleted in all trace elements (Fig. 7c) but Ni and Cr.

Augite (Aug), as euhedral to sub-euhedral crystals (Fig. 8), is sporadically found in basalts and basaltic andesites (0–3 area %) (Appendix B) where it is often strongly fractured, with common inclusions (eg. OS123) of plagioclase (An_{77-66}) and olivine (Fo_{70}) (Appendix C). It is commonly associated within glomerocrysts. Augite in dacites and diktytaxitic enclaves (0.14–14.31 area %) occurs as euhedral crystals with common inclusions of titanomagnetite or apatite and no fracture. Rims of pigeonite (OS123) and hourglass zoning or twinning were locally observed. Core compositions are imperfectly in equilibrium (Kd = 0.28 ± 0.08; Putirka (2008)) with their respective host bulk rock composition (Fig. 8a). Values of augite Mg# (molar Mg/(Mg + Fe$_{total}$) (Fig. 8b) in basalts and basaltic andesites ($Mg\#_{82-61}$) are similar to those of individually mounted crystals from pyroclasts ($Mg\#_{79-72}$) and higher than dacitic ones ($Mg\#_{70-50}$).

Pigeonite (Pgt) is commonly present in basalts and basaltic andesites, as microliths or as reaction rim around other pyroxenes or olivine ($Mg\#_{70-53}$) (Fig. 8b). Two occurrences included in plagioclase were analyzed in Hdw dacite ($Mg\#_{56-45}$).

Orthopyroxene (Opx) is found in the most evolved basaltic andesites ($Mg\#_{70-60}$) and in the dacites ($Mg\#_{60-50}$) (Fig. 8b) with textures similar to those of augite in dacites. It forms large euhedral and strongly fractured crystals in the evolved basaltic andesites (Fig. 8d,e) and is also found in reaction rims surrounding olivine. Its proportion remains relatively low, from trace amounts in some basaltic andesites up to ≤2
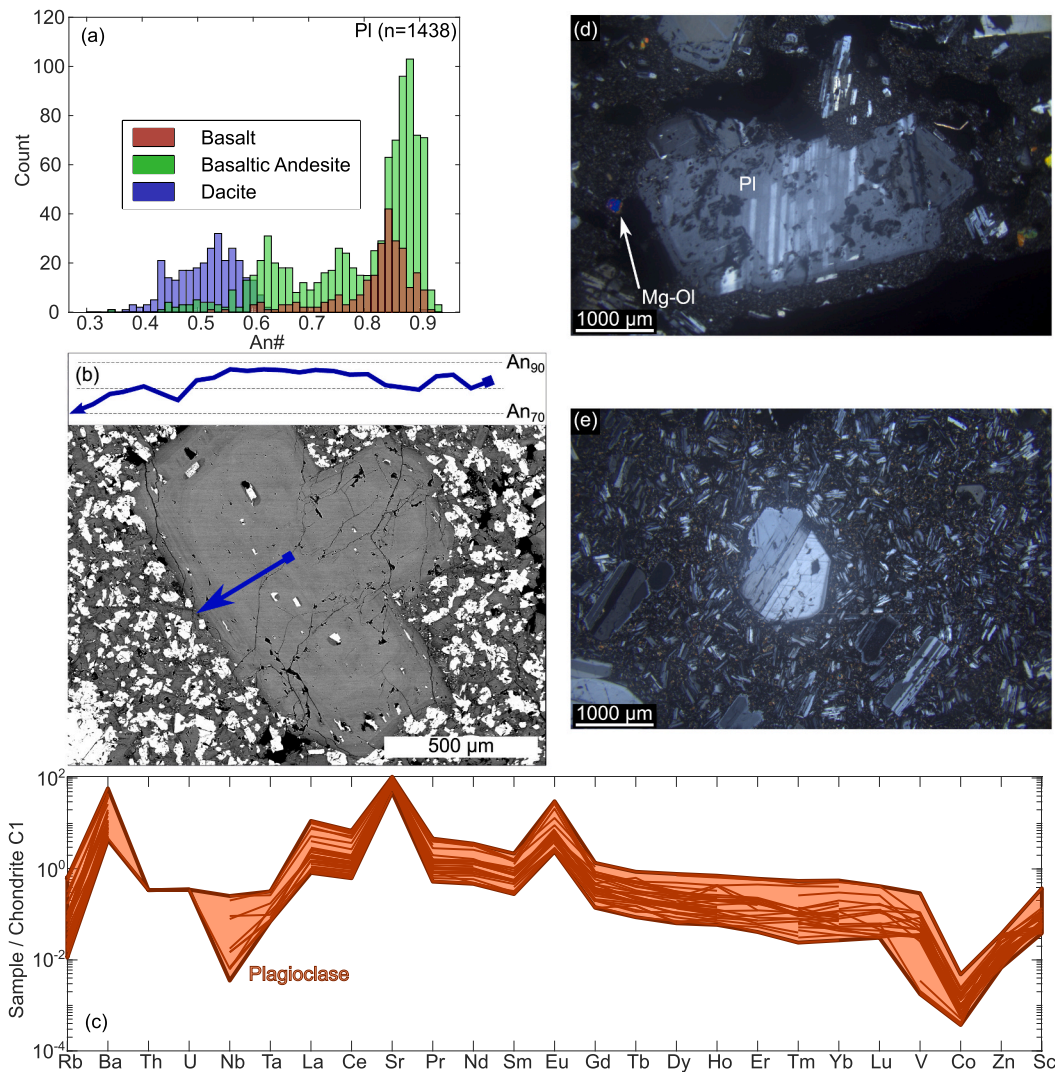
Fig. 6. Plagioclase textures and compositions. (a) An# content of EMPA plagioclases; (b) zoned plagioclase (BSE image) and profile from core to rim; (c) LA-ICP-MS spiderdiagram normalized to C1 chondrite (Sun Sun and McDonough, 1989), the basaltic matrix (Fig. 5) is added for comparison; (d), (e) microphotographs (crossed polars) of a complex sieved phenocrystal and a plagioclase dominated thin section, respectively.

area % in dacites (Fig. 8f) or diktytaxitic enclaves. Orthopyroxene is absent in the Fe-rich olivine bearing dacite (Hde). Dacite-hosted pyroxenes are richer in REE and Y, as well as poorer in Cr, V and Pb by an order of magnitude compared to the basaltic andesites-hosted crystals.

Amphibole (Amp), found in trace proportions and only in the Hdw dacite, is a brown pargasite (Fig. 9) according to the chemical classification of Hawthorne et al. (2012); Locock (2014). Crystals are generally surrounded by an oxide rim. Only one crystal with typical elongated shape and cleavage was observed, other crystals being smaller, often rounded and displaying no cleavage. Amphibole is also present in the Hdw diktytaxitic enclaves, in greater proportions. The amphiboles are rich in Sc, MREE and HREE compared with the basaltic matrix (Fig. 9c).

Opaques: Cr—Al spinels (Chr) (molar Al + Cr ≥20%; Fig. 9, 7d) are present in the less evolved basalts as dark brown cubes in olivines or within the matrix. The Cr# (molar $Cr^{3+}/(Cr^{3+}+Al^{3+})$) and Fe# (molar $Fe^{2+}/(Fe^{2+}+Mg^{2+})$; assuming stochiometry) are respectively 0.4–0.8, 0–0.8, 0–0.6 and 0.3–0.85, 0.7–0.9, 0.3–0.8 in the basalts, basaltic andesites and Cordon Cenizos samples. **Fe—Ti oxides** occur in all thin sections, mostly as black squared minerals in the matrix, but also as, often larger (up to 700 μm), crystals included in other phases (Figs. 7, 9). Titanomagnetite (Ti-Mag) is the principal oxide that locally shows bands of exsolution between magnetite (Mag) and ilmenite (Ilm) in the dacites

and in some basaltic andesites (Fig. 9b). Oxides rimming amphibole were also observed. The total proportion of opaque minerals ranges from 0.8 to 3.4 area % in diktytaxitic enclaves and from 0 to 1.3 area % in lavas, however this last value is likely underestimated due to the size thresholding at 100 μm. The trace contents of all opaque phases are similar (Fig. 9c), with enrichment in Nb and V relatively to the basaltic matrix.

Apatite (Ap) was only observed in the dacites (Figs. 7, 8, 9), as inclusions in other minerals or within the matrix as tiny (<10 μm) needles or grains. Its proportions vary from trace amounts in all dacites to 2.34 area % in diktytaxitic enclaves (Fig. S1). Like opaques, these proportions are likely underestimated due to the small size of the crystals.

Diktytaxitic enclaves (Fig. 9f,g) were counted as a mineral phase as they represent a substantial part of the samples (0.5–4.6 area %). They are mostly found in dacites (sizes up to 5 mm), but small ones were also identified in one basaltic andesite (OS32, up to 1 mm). Their reconstructed compositions are lower or equal in SiO_2 (Hde, 67.6 ± 0.3 wt%; Hds1, 62.1 ± 0.8 wt%; Hds2, 57.3 ± 0.8 wt%; Hdw, 58.8 ± 0.8 wt%) than their respective host rock (Hde, 67.9 wt%; Hds, 68.6–69.2 wt%; Hdw, 63.6–66.5 wt%) (Figs. 2 and 3). Their mineral content is similar to the host rock but crystals have acicular to prismatic shapes. A secondary Si-rich phase and few (Na,K)Cl crystals were observed in the porosity but
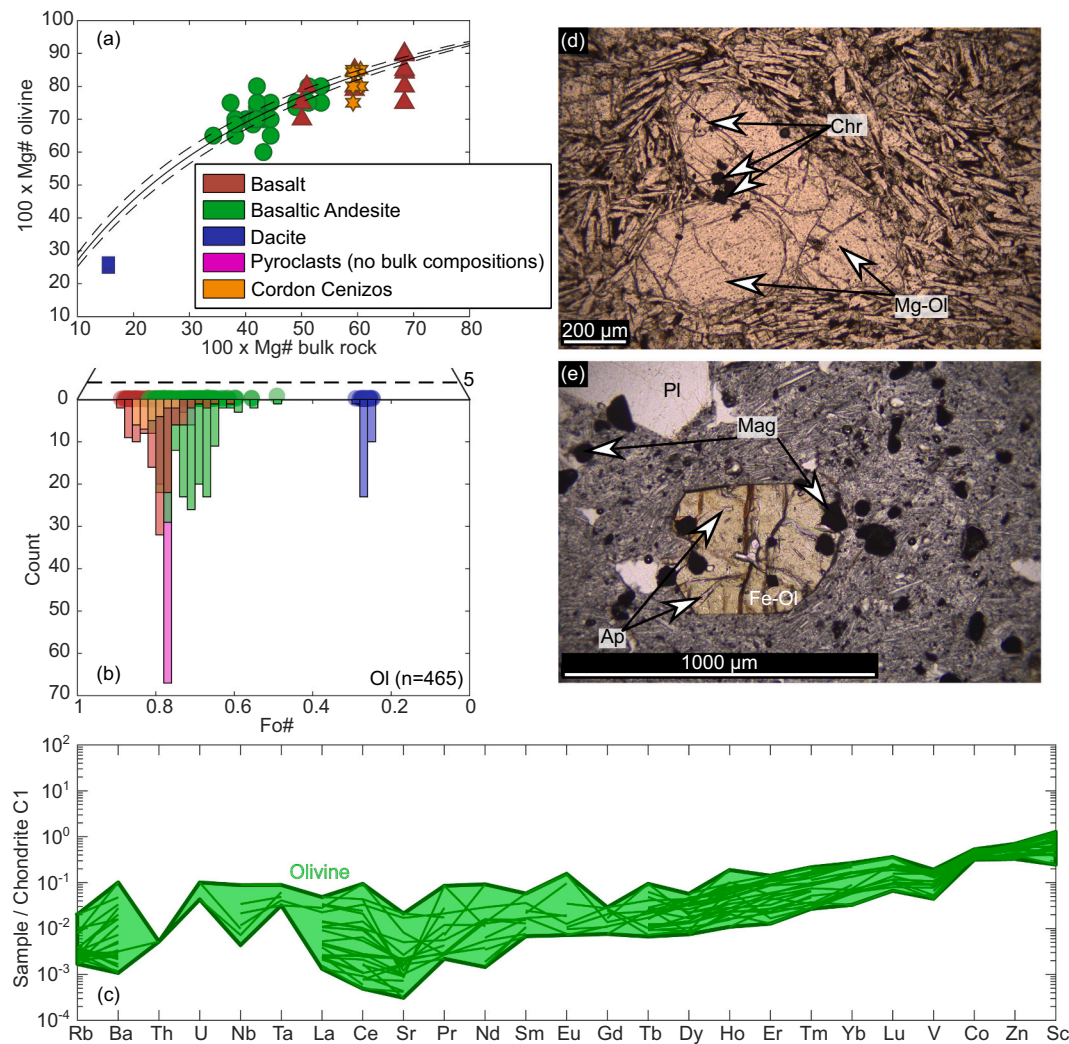
Fig. 7. Olivine textures and compositions. (a) Rhodes diagram testing equilibrium between olivine cores ($n = 138$) and host bulk rock composition; (b) Fo# from EMPA; (c) LA-ICP-MS spiderdiagram normalized to C1 chondrite (Sun and McDonough, 1989), the basaltic matrix (Fig. 5) is added for comparison; (d) and (e) microphotographs (parallel polars) of olivine crystals from a near-primary magma and a dacite, respectively.

were not further studied.

5. Modelling and discussion

5.1. Fractional crystallization

The occurrence of bell-shaped trends (Appendix D) in the TiO_2, Fe_2O_3, P_2O_5, V, as well as Zn Harker diagrams and the lack of mingling textures preclude mixing being a significant process. However, in the dacites, the presence of diktytaxitic enclaves indicate that this process locally took place. To quantitatively constrain the previous qualitative work of Lopez-Escobar et al. (1992), a fractional crystallization process was modeled with a five steps mass balance using a least square (LSQ) regression (Tables S12-S13). We started from a primitive basaltic composition (OS82) and tried to reproduce the compositions of progressively more evolved magmas: basalt (OS108), basaltic andesites (OS63, OS64, OS36) and one Hdw dacite (OS72). These samples were selected because they define a clear trend in most Harker diagrams (see Table S13). The phases that were considered in the model are plagioclase, olivine, clinopyroxene, orthopyroxene, Cr-rich spinel, titanomagnetite and apatite. The composition of the bulk cumulates was calculated using the modal mineral proportions obtained with the least square regression and mineral compositions (Tables S3-S7). Results are

presented in Table S13 and summarized in Tables 1 and 2. The overall fractionation from the primitive basalt to the Hdw dacite requires the crystallization of ≈ 88 wt% of the initial mass. Steps 1, 2, 3, 4 and 5 fractionate respectively 11, 23, 32, 42 and 55 wt% of troctolitic (75 wt% olivine, 25 wt% plagioclase), gabbroic (26 wt% olivine, 50 wt% plagioclase, 24 wt% clinopyroxene or 12 wt% olivine, 65 wt% plagioclase, 20 wt% clinopyroxene, 2 wt% titanomagnetite) and gabbronoritic (67 wt% plagioclase, 9 wt% clinopyroxene, 5 wt% titanomagnetite, 19 wt% orthopyroxene, traces of apatite or 62 wt% plagioclase, 16 wt% clinopyroxene, 11 wt% titanomagnetite, 10 wt% orthopyroxene, 1 wt% of apatite) cumulates. Sums of the squared residuals ($\sum r^2$) are below 0.08 except for first step (1.1) where we forced the system not to crystallize clinopyroxene in order to fit to petrologic observations. Not doing so improves $\sum r^2$ (0.02) but requires to precipitate 37 wt% of clinopyroxene. Major and trace elements were deduced by mass balance by withdrawing the cumulate from the starting composition in F (fractionation rate) proportions. Using the measured trace element compositions of minerals, an additional test was made using the Rayleigh distillation law (F taken from the least square model) and bulk partition coefficients ($\overline{D}$; see supplementary material). The relative error from calculated major element compositions (Table S13) is better than 6% except for some incompatible oxides: K_2O ($\leq 23\%$), P_2O_5 ($\leq 30\%$). For trace elements, the compositions predicted with mass balance agree
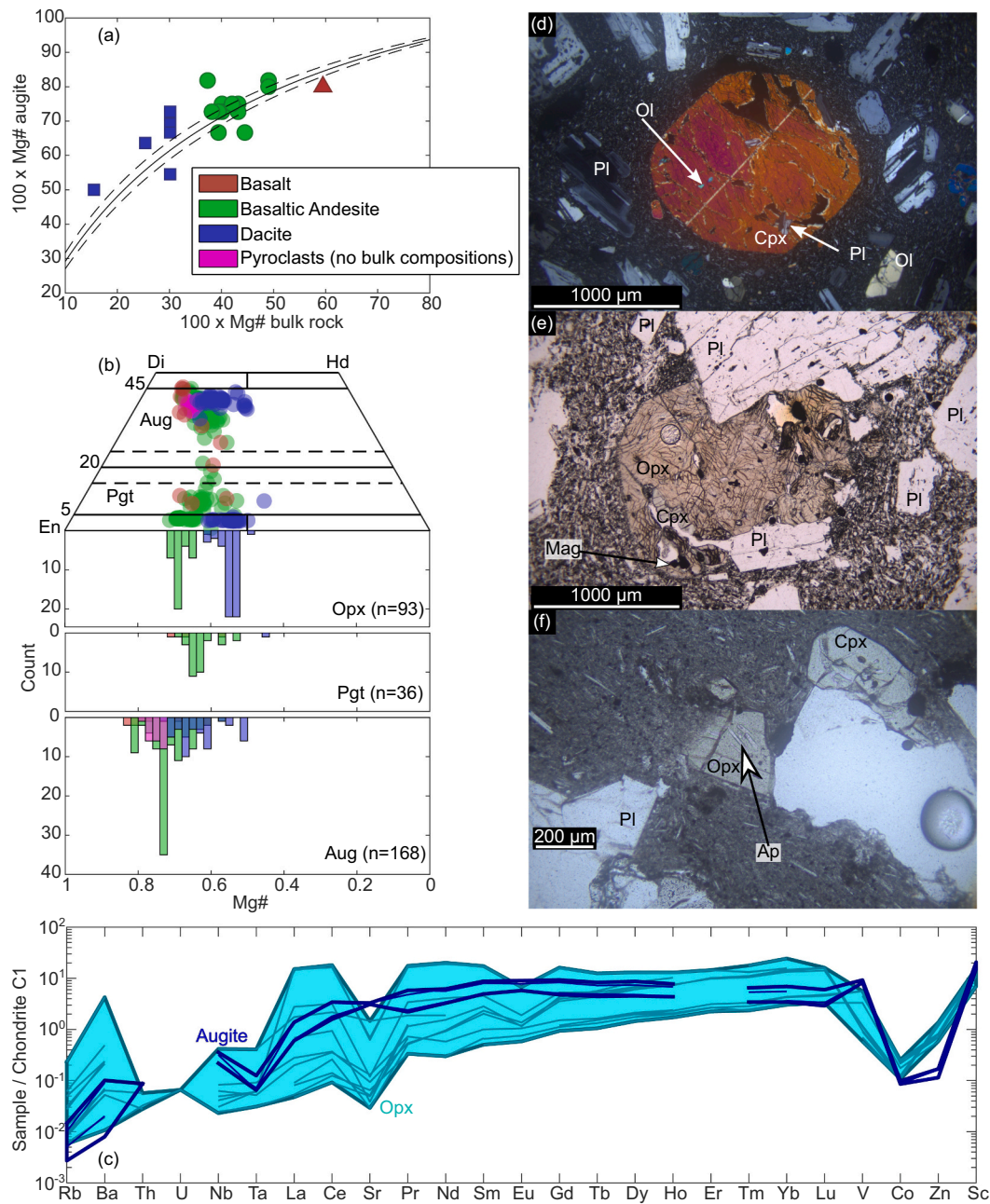
Fig. 8. Pyroxenes textures and compositions. (a) Rhodes diagram (Putirka, 2008) of augite cores and corresponding host rocks; (b) Ca, Fe, Mg ternary diagram for pyroxenes and Mg# of augite, pigeonite and orthopyroxene; (c) LA-ICP-MS spiderdiagram normalized to C1 chondrite (Sun and McDonough, 1989), the basaltic matrix (Fig. 5) is added for comparison; (d), (e) clino- and orthopyroxenes in basalt or basaltic andesite; (f) clino- and orthopyroxenes in dacite. (d) and (e), (f) are respectively in crossed and parallel polars.

rather well with observed compositions, with a better match in steps 1 to 3 then in steps 4 and 5 where MREE and HREE are too high and V too low. The errors in V can be explained by the lack of LA-ICP-MS measurements of the titanomagnetite (the required spot size was generally too large to properly measure the small oxides). For composition predicted using the Rayleigh equation, Zn is far too low in steps 4 and 5.

5.2. Melt water content estimate

Data on the volatile content of melt inclusions are currently lacking. The melt H_2O content has thus been estimated with petrological data using three different approaches: the Rayleigh distillation law, the Waters and Lange (2015) hygrometer and the Mandler et al. (2014) test.

5.2.1. Using the Rayleigh distillation law

We assume that H_2O behaves as a perfectly incompatible element because amphibole is the only hydrous mineral phase at Osorno and it is observed only in trace amounts in the Hdw dacite. The bulk partition coefficient of H_2O between cumulates and melt is thus close to zero. The Rayleigh distillation law can be used to calculate the water content along the differentiation trend if the water content of one composition and the fraction of residual liquid (f) are known (Vander Auwera et al., 2021): $f = C_0/C_L$ where C_0 and C_L are respectively the content of element I in the parent liquid (OS140) and in any other residual liquid L. f can be determined from bulk rock composition ($f = C_0^{Zr}/C_L^{Zr} = C_0^{H_2O}/C_L^{H_2O}$ where C_0^{Zr} and $C_0^{H_2O}$ are the Zr and H_2O content of OS140 and C_L^{Zr} and $C_L^{H_2O}$ the Zr and H_2O content in the resultant liquid). Results were fitted so as to obtain a unique value of f for every value of SiO_2 (Appendix E). In order
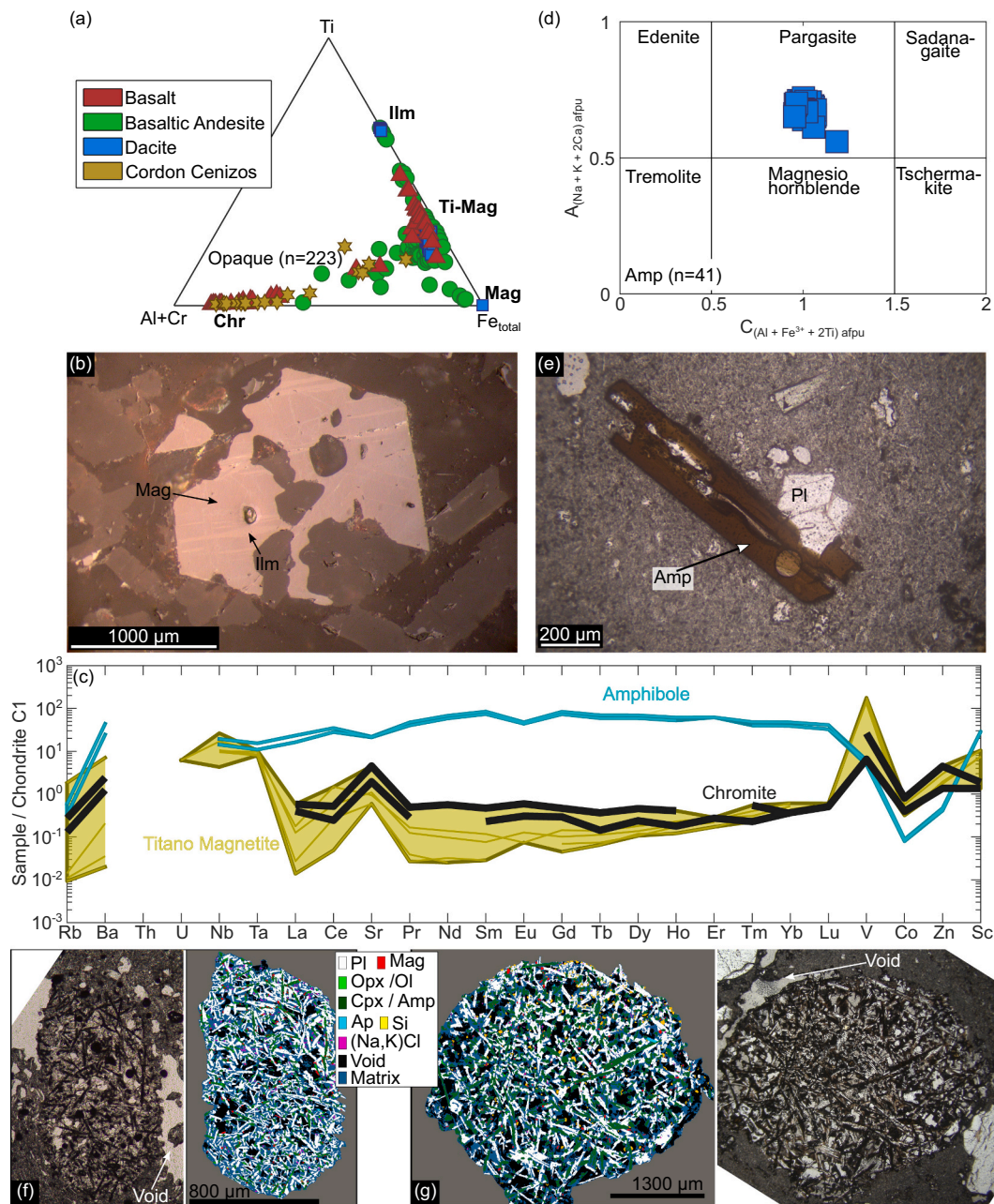
Fig. 9. Opaque, amphibole and enclaves textures and compositions. (a) Al + Cr, Ti, Fe ternary diagram; (b) reflected-light microphotograph of a titano-magnetite displaying ilmenite exsolutions; (c) LA-ICP-MS spiderdiagram normalized to C1 chondrite (Sun and McDonough, 1989), the basaltic matrix (Fig. 5) is added for comparison; (d) amphibole classification after Hawthorne et al. (2012); Locock (2014); (e) the largest amphibole crystal observed in Hdw dacite; (f) and (g) photomicrographs (parallel polars) of Hde and Hdw enclaves and their respective segmentation.

to determine $C_0^{H_2O}$, it is necessary to calibrate this fit ($r^2 = 0.78$, Standard Error Estimate [SEE] = ± 0.1) with one value of $C_L^{H_2O}$. In the Hdw dacite, amphibole is present only in trace amount ($X_{amp} \approx 0$), hence the bulk partition coefficient of H_2O ($D_{bulk} = X_{amp}.D_{amph}$) is likely to remain below 1. A Hdw-like paragenesis (Pl + Opx + Mag + Cpx + Amph) has been experimentally reproduced by Costa et al. (2004) who used the Tatara-San Pedro dacite, very similar to Hdw dacite OS136 (66 wt% SiO_2), as a starting composition. Their results at a pressure of 2 kbar and at NNO oxygen fugacity (conditions consistent with Díaz et al. (2020); Morgado (2019); Vander Auwera et al. (2019)) suggest that the Hdw dacite paragenesis can be reproduced in a very narrow temperature range (900–920°C) and H_2O content (between 4 and 5 wt%). Based on these experimental data, we considered that 4.5 ± 0.5 wt% H_2O was necessary to crystallize amphibole in the Hdw dacitic dome ($C_L^{H_2O} = C_{OS136}^{H_2O} = 4.5$

± 0.5 wt% H_2O; Fig. 10). It results in an initial water content ($C_0^{H_2O} = C_{OS140}^{H_2O}$) of 0.9 (+0.54 or -0.46) wt% H_2O at 50.5 wt% SiO_2 that increases to ≈ 2.70 (+1.64 or -1.36) at 58 wt% SiO_2 before the gap (Fig. 10). Expected values for andesitic compositions within the Daly gap are shown for information. Water saturation was calculated with VOLATILCALC (Newman and Lowenstern, 2002) at 5.76 wt% H_2O for a rhyolitic composition (the interstitial glass of the Hdw dacite is indeed rhyolitic) at 900°C and 2 kbar. Amphibole was not observed in the other dacitic units (Hds and Hde) suggesting that they formed at lower pressure and lower water content. Amphibole breakdown in dacites can be triggered by a temperature increase or by a decrease in pressure and water content (Costa et al., 2004; Ridolfi et al., 2010; Rutherford et al., 1985). Díaz et al. (2020) estimated that a dacitic reservoir was present

Table 1

Mass Balance Results. See supplementary tables 12 and 13 for more details.

Step	Step1 (cpx)	Step1 (no cpx)	Step2	Step3	Step4	Step5
L0	OS82	OS82	OS108	OS63	OS64	OS36
L1	OS108	OS108	OS63	OS64	OS36	OS136
L1 calc (error) in wt%						
SiO2	51.26 (0.01)	51.38 (−0.10)	52.55 (−0.16)	54.51 (−0.03)	57.15 (−0.21)	66.52 (−0.03)
TiO2	0.82 (0.01)	0.79 (0.04)	1.02 (−0.05)	1.12 (0.00)	1.26 (0.04)	0.49 (0.10)
Al2O3	17.92 (0.01)	17.35 (0.57)	18.52 (−0.04)	17.48 (−0.01)	16.36 (−0.09)	15.97 (−0.05)
MgO	7.12 (0.00)	7.14 (−0.02)	5.31 (−0.03)	4.07 (0.01)	2.75 (0.04)	0.89 (0.03)
CaO	10.09 (0.00)	11.05 (−0.96)	9.51 (0.03)	7.82 (0.02)	6.41 (−0.02)	3.80 (−0.03)
K2O	0.40 (0.06)	0.37 (0.09)	0.59 (−0.09)	0.71 (−0.13)	0.92 (−0.01)	1.89 (−0.21)
Na2O	2.55 (−0.16)	2.41 (−0.02)	2.66 (0.33)	3.48 (0.20)	4.00 (0.32)	4.78 (0.18)
Fe2O3T	9.57 (0.04)	9.25 (0.36)	9.49 (0.03)	10.39 (0.00)	10.68 (−0.05)	5.36 (−0.04)
MnO	0.16 (0.00)	0.15 (0.00)	0.15 (0.00)	0.17 (0.01)	0.19 (−0.01)	0.11 (0.02)
P2O5	0.12 (0.03)	0.11 (0.04)	0.19 (−0.01)	0.26 (−0.06)	0.29 (−0.02)	0.19 (0.03)
Σr^2	0.02	1.10	0.08	0.03	0.04	0.02
Phase compositions						
Chromite (Cr#)	46	46	–	–	–	–
Olivine (Fo#)	87	87	73	73	70	–
Plagioclase (An#)	87	87	74	73	72	42
Clinopyroxene (Mg#)	82	–	72	72	72	67
Titano-Magnetite (%Uvsp)	46	46	45	74	50	50
Orthopyroxene (Mg#)	–	–	–	–	68	51
Apatite*	–	–	–	–	Azufre	Azufre
Substracted Phases (%)						
Chromite	0.4	–	–	–	–	–
olivine	40.9	74.9	25.8	12.4	–	–
Plagioclase	21.5	25.1	50.2	65.4	66.7	62.0
Clinopyroxene	37.1	–	24.0	20.2	9.3	16.3
Titano-Magnetite	–	–	–	1.9	4.8	10.6
Orthopyroxene	–	–	–	–	19.1	10.4
Apatite	–	–	–	–	0.2	0.8
F**	0.82	0.89	0.77	0.68	0.58	0.45
F_{total}***	–	0.89	0.68	0.46	0.27	0.12
1-F_{total}	–	0.11	0.32	0.54	0.73	0.88

errors = measured value - modeled value.

Σr^2 = sum of the squared residuals.

* Apatite composition was taken from Tormey et al. (1995) at Azufre.

** residual melt after step i (i = 1 to 5).

*** overall residual melt from L0 in step 1 (no cpx).

under Osorno at 1–2 kbar. The water saturation calculated at 1 kbar (for a rhyolitic composition, 900°C) is only of 3.74 wt% H_2O (Newman and Lowenstern, 2002) which is indeed insufficient to crystallize amphibole (Costa et al., 2004; Ridolfi et al., 2010). For this reason, the estimated H_2O content of Hde and Hds dacites will be fixed at saturation levels at 1 kbar.

The methodology used here is based on the estimated H_2O content of the Hdw dacite that is back calculated to the basalt with the distillation model (Table S15). However, if volatile saturation was reached in the storage region, a fluid phase containing H_2O was exsolved during differentiation and our estimations would thus represent minimum values for the parent magma. The VOLATILCALC program (Newman and Lowenstern, 2002) predicts vapor saturation at 4.6 H_2O wt% for a basalt (49 SiO_2 wt%) emplaced at 2 kbar and 1100°C. If such an amount of water had been reached in the Osorno basaltic melt, amphibole would have been present in most of the erupted products as it is the case at Calbuco (Vander Auwera et al., 2021). Nevertheless, as CO_2 is likely present in the Osorno magmatic system and has a lower solubility, some H_2O could have been partitioned in a CO_2-dominated fluid phase. Results from this methodology have thus been tested with two other methods.

5.2.2. Using the Waters and Lange hygrometer

The Waters and Lange (2015) hygrometer (Table S14) was applied to basalts, basaltic andesites, andesite and the Hdw, Hds, Hde dacites using

respectively $An_{85\pm5}$, $An_{80\pm10}$, $An_{65\pm5}$, $An_{52\pm6}$, $An_{58\pm6}$, $An_{46\pm4}$. These values and associated errors correspond to the range of measured plagioclase core compositions, except for the dacites where it represents the mean ($\pm1\sigma$) of plagioclase cores (Table S4). Temperatures were calculated with eq. 16 from Putirka (2008) which is based on melt composition, except for dacites where we assume a temperature equal to 920°C (Costa et al., 2004, temperature where all observed phases are stable). A pressure of 2.5 ± 1.5 kbar was used (see Section 5.3). For the dacites, results from this hygrometer overlap those obtained with the previous methodology (Fig. 10). However, for the basalts and basaltic andesites, results range from about 1.6 wt% H_2O up to 6.3 wt% H_2O (excluding one outlier) if we use the complete whole-rock dataset but near-primary basalts. H_2O contents higher than the saturation level (4.6 wt%) are unrealistic. Moreover, if the basalts had >3 wt%, this would have been enough for amphibole saturation as in Calbuco (Vander Auwera et al., 2021). The Waters and Lange (2015) hygrometer strongly depends on melt composition as well as temperature, the latter being calculated here with empirical regressions that also depend on melt composition. We note that water contents above 4 wt% are obtained for the whole-rock compositions that have >18.5 wt% Al_2O_3. However, these high Al_2O_3 are above the trend modeled with the least square regression model (maximum 18.48 wt% Al_2O_3) and possibly result from slightly different crystallization conditions (the samples with high Al_2O_3 also have low MgO as discussed by Vander Auwera et al., 2019). If we apply the hygrometer only to the samples selected for the least square

Table 2

Trace element verification, more details in supplementary tables 12 and 13.

Step	Step1 (cpx)	Step1 (no cpx)	Step2	Step3	Step4	Step5
Calculated L1 (error) trace composition in ppm using LA-ICP-MS mineral analyses						
Sc	32 (1)	36 (−3)	35 (−4)	34 (−3)	33 (−3)	26 (−10)
V	191 (29)	213 (7)	250 (−28)	206 (38)	74 (134)	−671 (690)
Co	27 (7)	25 (9)	26 (4)	25 (1)	17 (4)	8 (−3)
Zn	54 (21)	52 (24)	78 (1)	93 (0)	100 (4)	91 (−10)
Rb	11 (1.41)	10 (2.18)	16 (−3.54)	18 (−6.48)	20 (4.04)	53 (−3.53)
Sr	369 (−14)	351 (4)	370 (30)	473 (−92)	349 (−8)	214 (59)
Ba	104 (27)	97 (34)	166 (−14)	217 (−49)	280 (−24)	504 (−82)
Ce	8.4 (3.8)	7.9 (4.3)	15.6 (−0.7)	21.3 (−4.5)	28.1 (−3.1)	52.6 (−13.7)
Eu	0.77 (0.04)	0.75 (0.07)	0.99 (0.00)	1.37 (−0.21)	1.85 (−0.44)	1.88 (−0.54)
Sm	2 (0.41)	2 (0.50)	3 (−0.24)	4 (−0.71)	6 (−0.93)	10 (−4.29)
Yb	1.6 (0.1)	1.6 (0.2)	2.2 (−0.2)	2.8 (−0.4)	3.8 (−0.7)	6.3 (−2.3)
Calculated L1 (error) trace composition in ppm using bulk partition coefficients and the Rayleigh distillation law						
Sc	29 (4)	36 (−3)	33 (−1)	33 (−2)	33 (−3)	20 (−4)
V	207 (14)	213 (7)	260 (−38)	257 (−12)	245 (−37)	95 (−76)
Co	30 (4)	29 (5)	29 (1)	29 (−3)	26 (−5)	17 (−12)
Zn	62 (14)	58 (17)	84 (−6)	89 (5)	76 (29)	44 (37)
Rb	11 (1.33)	10 (2.10)	16 (−3.65)	18 (−6.61)	20 (3.85)	53 (−3.39)
Sr	373 (−18)	356 (−1)	378 (21)	378 (3)	339 (2)	273 (1)
Ba	105 (26)	98 (33)	165 (−13)	209 (−41)	264 (−7)	487 (−65)
Ce	8.4 (3.8)	8.0 (4.2)	15.6 (−0.8)	20.7 (−4.0)	26.9 (−1.9)	43.5 (−4.6)
Eu	0.78 (0.03)	0.75 (0.06)	0.98 (0.02)	1.19 (−0.04)	1.42 (−0.02)	1.28 (0.07)
Sm	2 (0.43)	2 (0.49)	3 (−0.19)	4 (−0.65)	5 (−0.36)	5 (0.58)
Yb	1.6 (0.1)	1.6 (0.2)	2.1 (−0.2)	2.7 (−0.4)	3.7 (−0.6)	5.2 (−1.2)

errors = measured value - modeled value.

modelling, the calculated water content in the basalts and basaltic andesites ranges from 1.9 to 3.3 wt% (Fig. 10).

5.2.3. Using the Mandler et al. (2014) test

The water content can also be estimated using the Mandler et al. (2014) test (Table S14). This procedure combines empirical thermometers that are either dependent (eqs. 14, 15, 21, 22 of Putirka, 2008 assuming 1, 2, 3 or 4 kbar) or independent (eqs. 13 and 16 from Putirka (2008)) of the H_2O content of the liquid. The temperature calculated with the H_2O-dependent equations varies significantly with H_2O, whereas the temperature of the anhydrous equilibria is nearly constant. The intersection of the two groups of geothemometers gives an estimation of the water content. Results range from 0.4 to 1.8 wt% H_2O (Fig. 10; Table S14). The maximum H_2O content was selected for each basalt or basaltic andesite.

A moderate H_2O content (1.5 ± 0.75 wt% H_2O) in the basalts and basaltic andesites of Osorno agrees with melt inclusions data from Llaima (Bouvet de Maisonneuve et al., 2012; Ruth et al., 2016) (Fig. 10) and with the melt H_2O content estimated by Morgado (2019)(numeric modelling) on a basaltic andesite from Osorno. These values are lower than those estimated for the basalts (Vander Auwera et al., 2021, 3.0–3.5 wt%) and basaltic andesites (Namur et al., 2020, 3.5–4.5 wt%) of Calbuco, based respectively on petrological data and on the presence of An_{85-90} cores in plagioclase. However, this difference is supported by the absence of amphibole at Osorno (except from a few grains in one dacite) and its presence as a major phase at Calbuco (Sisson and Grove, 1993). The presence of anorthite-rich cores in plagioclase at Osorno could be interpreted as resulting from a high melt water content (Pichavant et al., 2002). However, Panjasawatwong et al. (1995) showed that other parameters such as a high melt Ca/Na ratio and/or a high melt Al_2O_3 content are also controlling the stability of anorthite in arc magmas. Moreover, Ulmer et al. (2018) obtained high An plagioclase in a basalt with 2.5 wt% H_2O. Consequently, it is possible that several parameters, including melt H_2O content, are interplaying and controlling the stability of anorthite in these basalts. Zimmer et al. (2010) indicated that tholeiitic arc basalts have <2 wt% H_2O in agreement with what is obtained here for the tholeiitic basalts of Osorno.

5.3. Thermobarometry

The *P* and *T* conditions of the main storage region were estimated

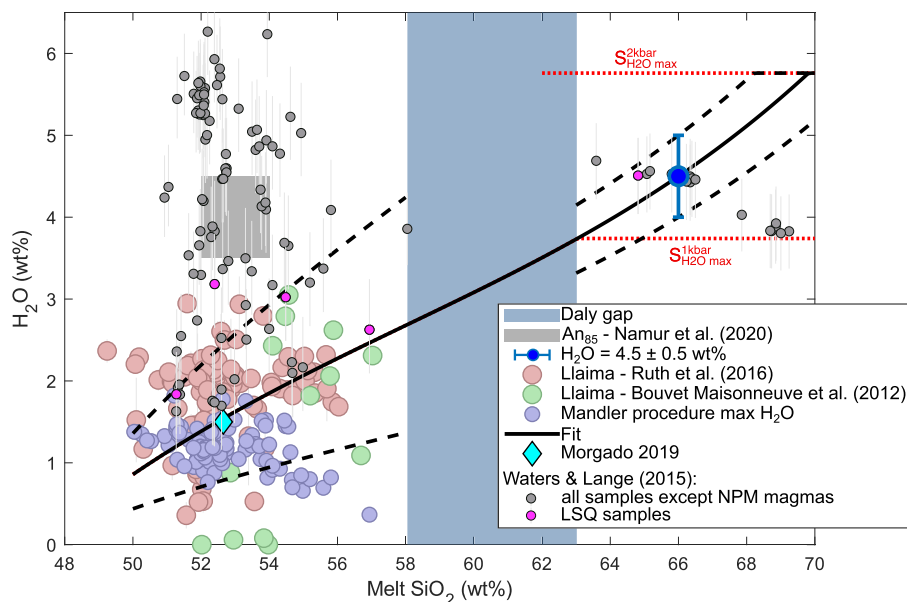**Fig. 10.** SiO_2 (wt%) vs calculated H_2O content (wt%). H_2O was calculated (solid line) assuming that H_2O behaves like Zr ($D^{H_2O} \approx 0$) and that 4.5 wt% (± 0.5, dashed black lines) H_2O was necessary (Costa et al., 2004) to crystallize traces of amphibole in the Hdw dacitic dome (66% SiO_2). Errors consider the assumed H_2O range and the SEE from f. Results agree with the H_2O content estimated in a basaltic andesite of H1835 by Morgado (2019). The small grey area shows the conditions required for the crystallization of high anorthitic plagioclase in Calbuco lavas (Namur et al., 2020). Llaima melt inclusions, Waters and Lange (2015) and Mandler et al. (2014) procedure results were added for comparison. See text for more details.

using several phase equilibria. As rocks are saturated with olivine, olivine-liquid equilibrium is expected. Therefore, liquid temperatures were calculated using eq. 14 (wt% $SiO_2 \leq 60$) from Putirka (2008) and our calculated water contents. Dacites being all saturated with clinopyroxene, the same rationale was used. Additionally, rhyodacitic melt compositions from EMPA were assumed in equilibrium with clinopyroxene. Saturation temperature was estimated with eq. 34 from Putirka (2008) (wt% $SiO_2 \geq 60$, assuming 1.5 ± 0.5 kbar; see Section 5.2 for justification) based only on liquid compositions and our calculated water contents. An error of 1 kbar results in temperature difference of $\approx 11°C$ with eq. 34, which is reasonable for the dacites. The selected liquid compositions are the bulk rocks, assuming that they represent liquid compositions, and the rhyolitic interstitial melt from the dacites. Resulting temperature (Table S16a) decreases with increasing SiO_2 (Fig. 11) starting at $\approx 1250°C$ for the basalts down to $\approx 1000°C$-$900°C$ for the dacites (1000°C-750°C considering interstitial melts) and 900°C-750°C for the rhyolitic interstitial melts.

We further tested equilibrium between each whole-rock composition and each clinopyroxene analysis (Kd = 0.27 ± 0.03 and $|DiHd_{predicted} - DiHd_{observed}| \leq 0.05$; Neave and Putirka (2017); Putirka (2008)). This resulted in 1293 equilibrium pairs. The thermometer proposed by Petrelli et al. (2020), based on machine learning and calibrated with experimental data, was used. It confirms the temperatures calculated with eqs. 14 (olivine-melt) and 34 (Cpx-melt) of Putirka (2008) (Fig. 10a).

The thermodynamic barometers of Putirka (2008) (eq. 32a) and Neave and Putirka (2017) as well as the two machine learning barometers (Cpx-liquid equilibrium and Cpx only) of Petrelli et al. (2020) were used to determine pre-eruptive pressures. There is no significant difference among results (Table S16b) obtained with the different barometers (Fig. 11) or between basalts, basaltic andesites and dacites, with a peak for the four calculations around 2.5–3.5 kbar (Putirka (2008), eq. 32a: median = 2.74 kbar, $\sigma = 1.03$ kbar; Neave and Putirka (2017): median = 2.74 kbar, $\sigma = 0.70$ kbar; Petrelli et al. (2020), Cpx-liquid: median = 3.31 kbar, $\sigma = 0.40$ kbar; Petrelli et al. (2020), Cpx only: median = 2.57 kbar, $\sigma = 0.86$ kbar). These results indicate that either the basalt and dacite differentiated at the same pressure or at pressures that differ by a value that is less than the resolution of most literature barometers (a few kbar).

5.4. Rhyolite-MELTS modelling

To test if the calculated pressures are realistic and fit with the natural data, rhyolite-MELTS (Ghiorso and Gualda, 2015; Gualda et al., 2012) was used to simulate fractionated crystallization of one of the five near-primary magmas from Osorno (OS83) at different pressures (5 to 1 kbar). Tests were performed at different oxygen fugacities: NNO, FMQ + 1, FMQ (Morgado, 2019; Vander Auwera et al., 2019), with an initial H_2O content of 0.5 to 2 wt% using isobaric conditions and temperature steps of 20°C (from 1300 to 800°C). A few runs were also realized in non-
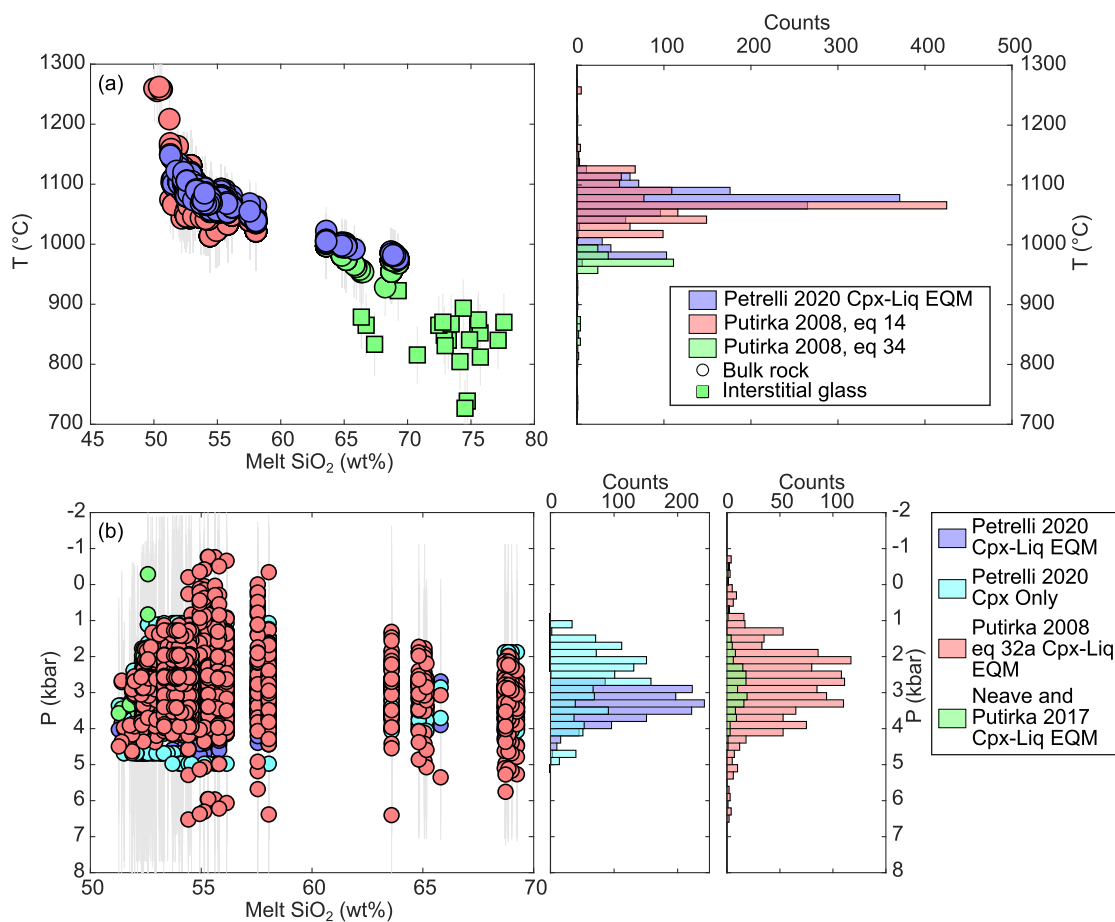

Fig. 11. Thermobarometry. (a) Temperature versus SiO_2 diagram and associated histogram. Temperatures were derived from the thermometers of Putirka (2008) (eqs. 14 and 34) and Petrelli et al. (2020). (b) Pressure versus SiO_2 diagram (note the absence of any significant change of pressure with SiO_2 content) and associated histogram. The barometers are from (Putirka, 2008) (eq. 32a), Neave and Putirka (2017) and Petrelli et al. (2020) (Cpx only and Cpx-Liquid). The large light grey bars take into account the errors on temperature, water content and SEE (Standard Error Estimate) for Neave and Putirka (2017) and Putirka (2008) and only the SEE for Petrelli et al. (2020). n for clinopyroxene-liquid pairs and liquid compositions are 1293 (for temperatures and pressures) and 143 (temperature), respectively. See text for further details.

isobaric conditions by implementing a linear pressure decrease from 3 to 1 kbar or 5 to 1 kbar in order to simulate polybaric differentiation of the magma. All simulations (Table S17 and supplementary large electronic figure) were compared with the observed mineralogy, major element chemistry, water content and estimated temperatures. Results obtained at a pressure ≥ 4 kbar are inconsistent (crystallization of garnet or leucite, predominance of pyroxenes over olivine and plagioclase) so are decompressing runs from 5 to 1 kbar. However, natural observations agree with results from runs at 3 kbar or less and with a decompression from 3 to 1 kbar.

Figs. 12, 13 summarize one of the best results which was performed at FMQ, 2 kbar and with an initial H_2O content of 1 wt%. The mineralogy prior the compositional gap is fairly well reproduced with Fo_{85-75} (olivine), An_{82-65} (An ≥82 are missing), $Mg\#_{80-65}$ (augite), $Mg\#_{70-65}$ (pigeonite), $Mg\#_{68-65}$ (orthopyroxene). After the Daly gap, results agree

also quite well with An_{60-40} (plagioclase), $Mg\#_{70-60}$ (augite), $Mg\#_{65-55}$ (orthopyroxene). Other parameters such as the main paragenesis composition, the order of appearance of the mineral phases, the temperature, the water content or even the residual melt fraction are also well reproduced. The modelling with rhyolite-Melts thus supports the low H_2O content of the basalts deduced from petrological data. Additionally, rhyolite-MELTS predicts a peak in crystallization when plagioclase first appears (Fig. 13 and Appendix F). This may explain the predominance of plagioclase observed in most lavas and the high cristallinity which is also fairly reproduced with rhyolite-MELTS. Some features that are not properly reproduced by the 2 kbar - FMQ - 1 wt% H_2O run are nonetheless predicted by other runs with a similar set of initial conditions: occurrence of an Fe-rich olivine (with less initial water or non-isobaric differentiation), a more anorthitic plagioclase, up to An85 (with more initial water) and apatite (with either less water or
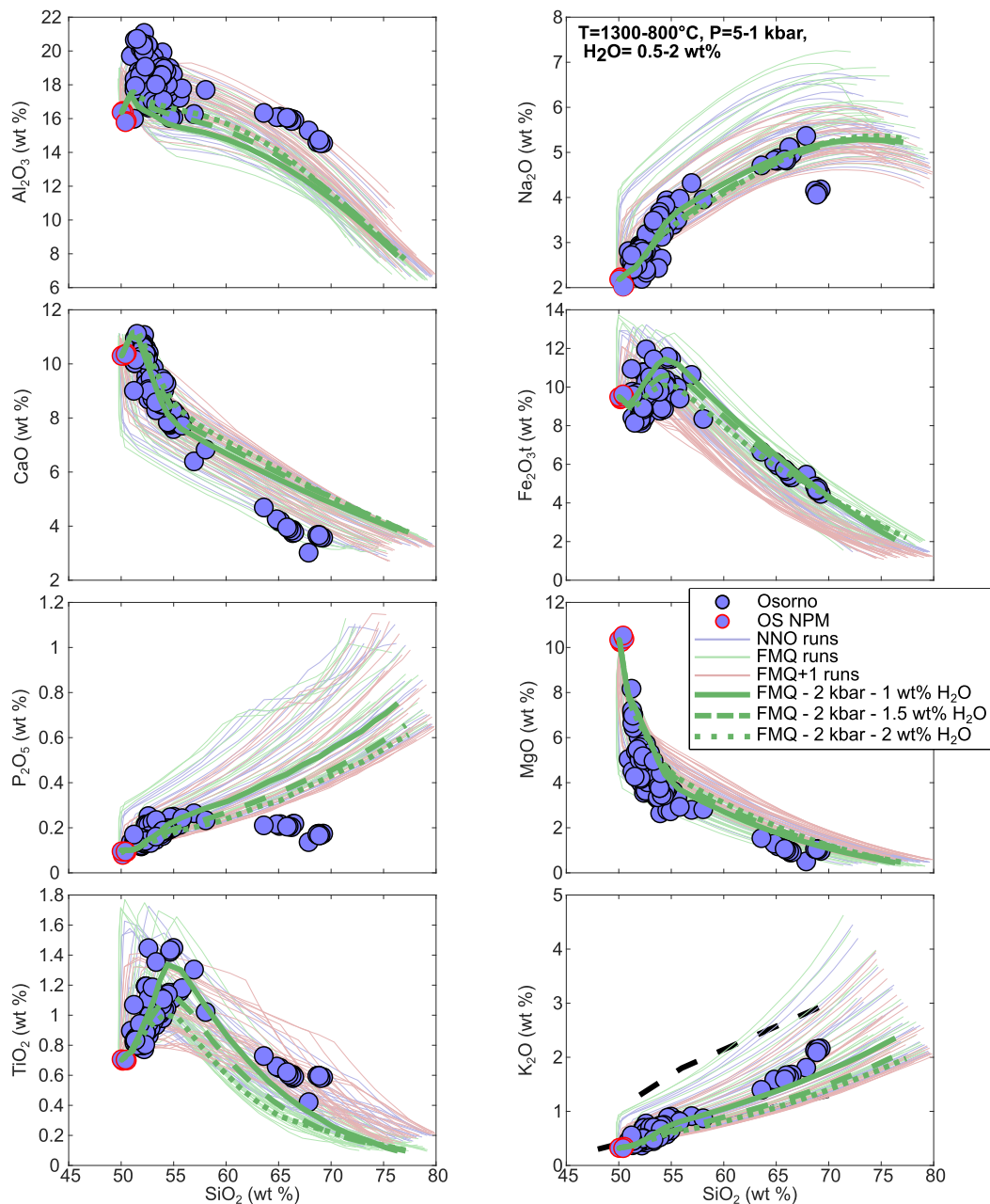

Fig. 12. rhyolite-MELTS runs results. The best fit, highlighted with the thick green line, is obtained at FMQ, 2 kbar and initial H_2O = 1 wt%. Two other runs with a higher H_2O content (1.5 and 2 H_2O wt%) are also emphasized. (For interpretation of the references to colour in this figure legend, the reader is referred to the web version of this article.)
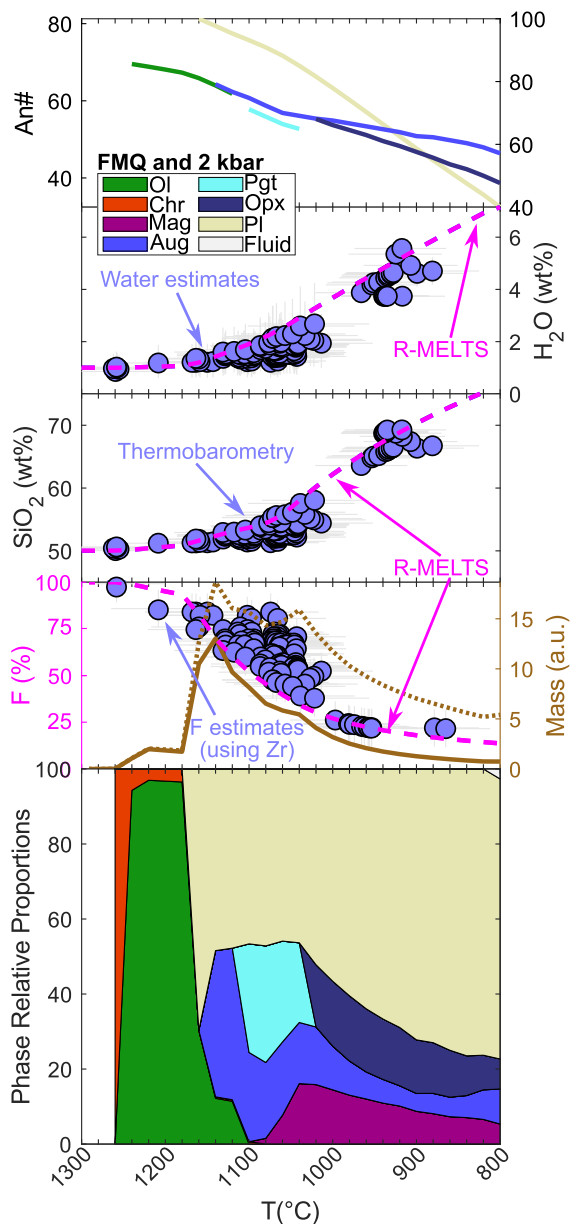
Fig. 13. Results of the best rhyolite-MELTS (Ghiorso and Gualda, 2015; Gualda et al., 2012) fractional crystallization simulation at 2 kbar (isobaric), FMQ and using sample OS83 as the starting composition with an initial water content of 1 wt%. From top to bottom, the panels display the Mg# (with Fe as total iron) of the ferromagnesians (olivine, Opx and Cpx) and the An of plagioclase as a function of temperature (T˚C). The second and third panels compare the results of rhyolite-MELTS with respectively the calculated H_2O content (see section 4.4) and temperature (see Section 4.5). The fourth panel shows crystallization data. The dotted and solid brown lines represent the mass that crystallized at each temperature step in rhyolite-MELTS, the relative to the residual mass of liquid or to the initial mass, respectively. The magenta dotted line compares the percentage of residual liquid (F) modeled with rhyolite-MELTS and calculated with Zr (filled circles, Fig. S5). The last panel represents the modal weight proportions of each phase crystallizing or exsolving (fluids) from the melt. The calculated liquidus temperature is 1260˚C, which means that conditions are above liquidus. Additional results about crystallinity are available in Fig. S6. (For interpretation of the references to colour in this figure legend, the reader is referred to the web version of this article.)

higher pressure or more reduced conditions). Finally, an overall fractionation of ≈ 77.5% (residual melt fraction f = 0.225) at 940˚C and approximately 69 wt% SiO_2 agrees very well with the one calculated using the Zr content (78.7% at 67 wt% SiO_2).

5.5. Magma storage below Osorno

Geochemical data (Figs. 2 to 4), modelling (mass balance, rhyolite-Melts) and geothermobarometry (Fig. 11) indicate that the chemical diversity of Osorno magmas was mainly produced by fractional crystallization of a parent tholeiitic basalt containing ca. 1 wt% H_2O in a storage region located at mid to upper crustal depths (ca. 4–11 km below the summit). The observed crystallization sequence in the basalts and basaltic andesites extends (Appendix G) the one previously proposed by Klerkx (1964). Cr-spinel and Mg-olivine crystallized first followed by plagioclase, clinopyroxene, titanomagnetite and late orthopyroxene. After the compositional gap, saturation of apatite is reached as it is found included in most minerals. The Hde dacite is the most evolved composition where orthopyroxene is replaced by fayalite, as also observed at the Puyehue-Cordon Caulle complex (Singer et al., 2008). A trace amount of amphibole in the Hdw dacite likely crystallized because of a slightly higher pressure (Marxer et al., 2021). The observed textures (crystal clots, intersertal matrix) agree with Tagiri et al. (1993) and Vander Auwera et al. (2019, 2021) who discussed the incorporation of crystal clots in an aphyric basaltic andesite in nearly cotectic proportions. This reconciles the complex textural observations with the chemical trends that follow the experimental liquid lines of descent. The database presented here on the eruptive products of Osorno (geobarometers, fractionating assemblage involving olivine, geochemical trends) indicate no sign of high pressure fractionation. This doesn't exclude the possibility that batches of magma fractionated at higher pressure, however our data indicate that these magmas did not erupt at Osorno.

In the basalts and basaltic andesites, the crystallinity is rather variable, from <10% up to >50% (Appendix F). However, the most evolved basaltic andesites, the andesites and the dacites have low crystallinities. Such observations were mentioned at La Picada by Vander Auwera et al. (2019) who suggested that the dacitic melt has been extracted from a crystal mush of basaltic andesite composition, thus creating the compositional gap. At Osorno, even if the Daly gap is also observed, its creation by such a process is not entirely satisfying as crystal poor basaltic andesites exist. However, crystal rich basalts are better candidates to form crystal-poor basaltic andesite or andesite by melt extraction. Coombs et al. (2002) explain the formation of mafic enclaves in dacites by the underplating of a hotter denser andesitic melt below a dacitic one. The mafic melt cools down, crystallizes and evolves which triggers volatile exsolution. Exsolved volatiles decrease melt density and allow the mingling of the two magmas. In this model, diktytaxitic enclaves result from the rapid cooling of the andesitic melt in the dacitic one. Then the thermal instability of andesitic compositions (Grove and Donnelly-Nolan, 1986) is a good candidate to explain the Daly gap at Osorno.

Using magnetotelluric data, Díaz et al. (2020) proposed that the storage region below Osorno extends from 1 to 6 kbar. Our results generally agree with this conclusion. However, we pointed out that at a pressure above 3 kbar, the proportion of pyroxenes in the cumulates significantly increases (rhyolite-Melts; large electronic figure), contradicting with petrographic observations on the basalts and basaltic andesites. Moreover, a narrower range of pressures is predicted by the thermomechanical model of Huber et al. (2019) stating that magma stalling preferentially occurs at 2 ± 0.5 kbar. Such pressures below Osorno also correspond to the intracrustal discontinuity (Tassara and Echaurren, 2012) that seem to play a role in the depth of most magmatic systems in the SVZ (Figs. 14, 15). Furthermore, during a seismic unrest below Osorno which occurred in 2018–2019 (Tables S19, Fig. 14, Appendix H) (Ortega, 2021), most of the seismicity was located at pressures
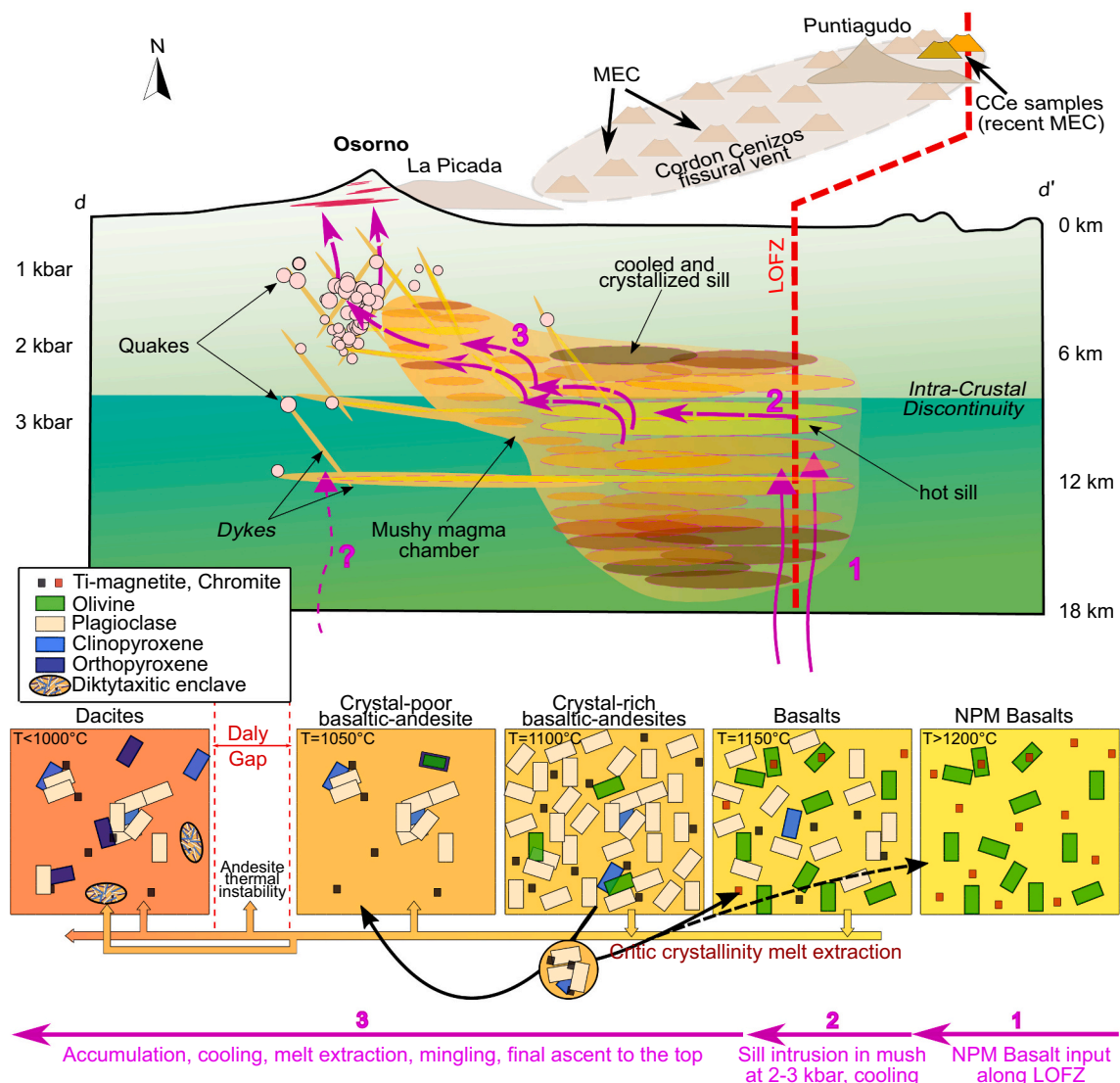
Fig. 14. Magma chamber model modified after Díaz et al. (2020). Most of the magma chamber is expected to be in a mushy state. Depth-pressure relations were estimated from the Tassara and Echaurren (2012) model (Table S18). Reported quakes (pink circles) are from Ortega (2021) (Table S19). The d-d' cross section is from Díaz et al. (2020) and is shown on Fig. 1. The proposed succession of events is as follows: (1) near-primary magmas or primitive basalts ascent through the LOFZ network; (2) at the depth of the intracrustal discontinuity, ≈ 7–8 km bsl corresponding to ≈ 2–3 kbar, the magma flow turns into a sill alongside the discontinuity and new incoming sills may push down older sills; (3) magma enters the uppermost chamber via sill and dyke network or through the mush via reactive melt flow process (Jackson et al., 2018). Dacitic compositions likely forms through melt extraction on top of the magma chamber or in NW fracture network (Vander Auwera et al., 2019). The small panels below the main figure show the global evolution of magma textures from primitive basalt to dacite if not erupted. Melt extraction window occurs in the basaltic or basaltic-andesitic fields when crystallinity reaches a threshold. (For interpretation of the references to colour in this figure legend, the reader is referred to the web version of this article.)

of 1–2 kbar on the edge of the magmatic chamber modeled by Díaz et al. (2020) (Fig. 14). The quakes (Ortega, 2021), interpreted here as resulting from the emplacement of dykes in the bedrock (Fig. 14) or in the magma storage zone, also indicate that the eruptible magma is emplaced at shallow depths (≤3 kbar). The deeper magmatic system modeled by Díaz et al. (2020) can be explained after Jackson et al. (2018) who numerically showed that a mushy storage system can be built by repeated intrusion of sills at a specific pressure. Their model successfully reproduces silicic melts from a basaltic one in mushy environments and also leads to the incremental vertical expansion of the storage area. This process could explain why most of the differentiation depths in the CSVZ emplaced at shallow pressures along the ICD discontinuity (Fig. 15).

6. Conclusions

In this study, we have produced a significant geochemical database representative of all units outcropping on Osorno. Based on this database, a model predicting the magmatic system below Osorno has been proposed. The ascent of the primary mantle melt to the upper crust was likely facilitated by the presence of the LOFZ near Osorno. The lavas and pyroclasts that finally erupted were differentiated in the upper crust where an intracrustal discontinuity has been identified. No evidence of high pressure fractionation was recorded in the mineral composition or in the differentiation trend. Indeed, the abundance of early crystallizing olivine followed, by plagioclase, can only be reproduced by fractionation at about 2–3 kbar which is corroborated by geophysical data. This low pressure agrees with results obtained for other volcanoes in the Central Southern Volcanic Zone that are either close to Osorno (Vander
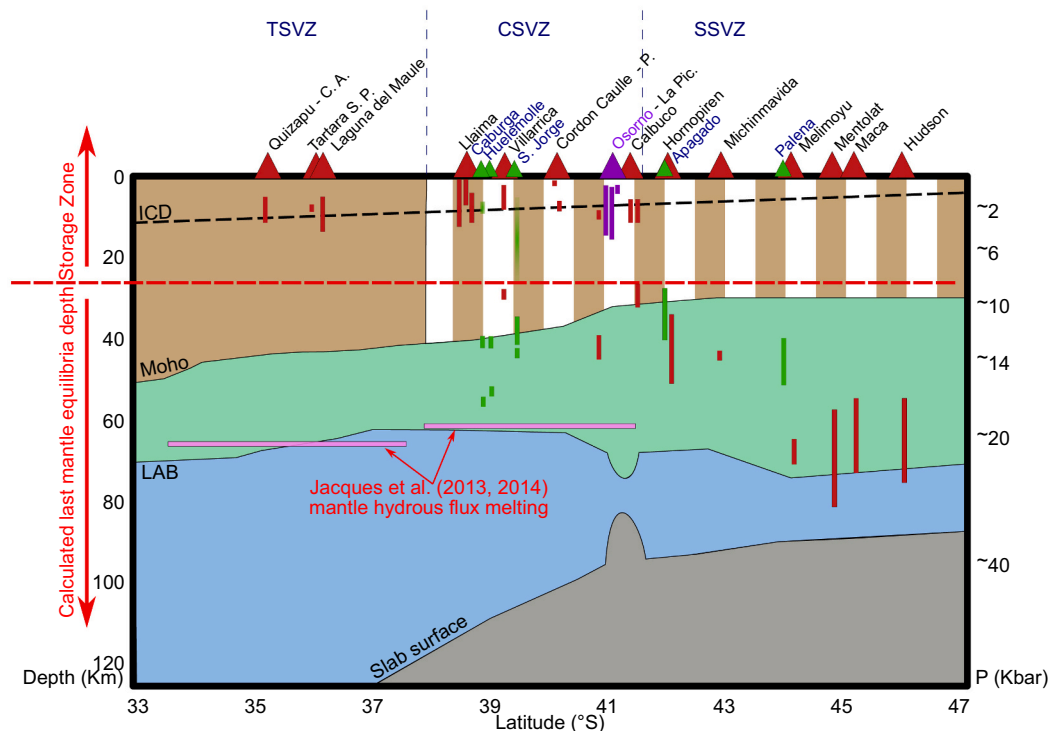
Fig. 15. Estimated depths for the main magma storage and last equilibration of the primary magma for some volcanoes across the SVZ. The background is modified after Hickey-Vargas et al. (2016b) (we chose not to use any smoothing equation). Depth / pressure relations were estimated after Tassara and Echaurren (2012) model. This model extending only down to Melimoyu latitude, the boundaries were extrapolated further south. The asthenosphere irregularity below Osorno and Calbuco is likely due to their position slightly forward the arc compared to other volcanoes. Green triangles and blue fonts refers to monogenic edifices while red triangles and black font shows stratovolcanoes. Purple emphasizes Osorno data. Pressures or depths are from Ruprecht et al. (2012) for Quizapu C.A., Costa et al. (2004) for Tartara S.P., Klug et al. (2020) for la Lagune de Maule, Hickey-Vargas et al. (2016a); McGee et al. (2019); Morgado et al. (2015, 2017) for the comparison of Caburga, Huelemolle, Villarrica and San Jorge group, Castro et al. (2013); Jay et al. (2014) for Cordon Caulle, Díaz et al. (2020); Morgado (2019); Vander Auwera et al. (2019) and this study for Osorno and La Picada, Morgado et al. (2019b, 2019d); Vander Auwera et al. (2021) for Calbuco; Watt et al. (2013) for Hornopiren, Apagado, Michinmuhuida or Palena and Weller and Stern (2018) for Melimoyu, Mentolat, Maca and Hudson. Rectangles without stroke represents transient reservoirs (Morgado et al., 2017). Horizontal stripes represents calculated mantle melting pressures by Jacques et al. (2013, 2014) for the TSVZ and CSVZ. ICD and LAB respectively means Intra-Crustal Discontinuity and Lithosphere Astenosphere Boundary. (For interpretation of the references to colour in this figure legend, the reader is referred to the web version of this article.)

Auwera et al., 2019, 2021) like Calbuco and La Picada or more distant like Villarrica and Llaima (Morgado et al., 2015; Ruth et al., 2016). The Osorno parent basalts apparently had a low water content (≈ 1.0 wt%) that is below the average for arc magmas (≈ 4 wt%; Plank et al., 2013). However, it is in concordance with their tholeiitic composition, as observed in other arcs such as the Aleutian volcanoes (Zimmer et al., 2010).

Supplementary data to this article can be found online at https://doi.org/10.1016/j.lithos.2022.106777.

Author contributions

Conceptualization: J.V.A., O.N., T.B; **Data curation:** T.B., J-L.D., N.D., M.B., H.F.; **Formal analysis:** T.B., M.B., H.F.; **Funding acquisition:** J.V.A., O.N., T.B.; **Investigation:** J.V.A., O.N., O.B., T.B., P.F., H.F.; **Methodology:** J-L.D., N.D., H.F., M.B., T.B.; **Project administration:** J.V.A; **Resources:** J-L.D., N.D.; **Software:** T.B.; **Supervision:** J.V.A., O.N., O.B.; **Validation:** T.B., J.V.A., O.N.; **Visualization:** T.B., P.F.; **Writing – original draft:** T.B., O.N., J.V.A, O.B.; **Writing – review & editing:** T.B., J.V.A., O.B., O.N., P.F.

Declaration of Competing Interest

The authors declare the following financial interests/personal relationships which may be considered as potential competing interests:

Olivier Namur reports a relationship with Research Foundation

Appendix A. Methodology

A.1. Point counting and segmentations

(1) Point counting analysis of 25 samples have been realized using a PELCON automatic point counter. Steps along x- and y- axis were set at http ://0.4.mm and a total of 1510–4464 points were counted for each thin section. Crystals ≤100 μm were included in the matrix. (2) A TUSCEN Michrome 6 camera was used to scan ten samples for digital classification of mineral populations. Segmentation was made by manually contouring minerals or adjusting colour thresholds. A minimum total of 543–9949 crystals were analyzed for each thin section. Crystal clusters of the same mineral were counted as a single crystal. (3) chemical map was made from sample OS136 (this sample is interesting because it possess a large enclave and scarce amphiboles) and some diktytaxitic enclaves (for bulk composition estimates) using a SEM JEOL JSM-6510 with EDX (Bruker-AXS XFlash, silicon drift detector) at the Centre de Recherches Pétrographiques et Géochimiques (CRPG, Nancy, France). Working distance was 10 mm with 20 keV accelerating voltage and a beam current of 10 nA. The phase segmentation followed the method of Drignon et al. (2016).

A false colour image isolating the various mineral phases was also produced for each analyzed enclave with the following method (adapted from Drignon et al. (2016)). Chemical maps (Al, Ca, Mg, Fe, Ti, Na, K, Si; Cl, BSE) were acquired at the SEM and, using ImageJ software, each image was threhsolded to select the regions rich in each element. High- and medium-Fe thresholds were applied for oxides and ferromagnesian minerals, respectively. When the contrast in Fe wasn't sufficient, all Fe was counted in medium-Fe. Images were binarized and, then, bolean operations were applied to segment each phase. The general group of all chemical images will be referred as Img. When Img_1 (all the chemical maps at the 1st step) appears, it means that previously segmented phases (apatite, oxides) were subtracted from all initial images. It ensures not to count any pixel twice.

- Oxides = high-Fe OR (medium-Fe AND Ti)
- Apatite = Ca AND P
- Img_1 = Img_0 SUBSTRACT (Oxides OR Apatite)
- CPX_Amph = Ca_1 And Mg_1
- Img_2 = Img_1 SUBSTRACT (CPX_Amph)
- OPX_Ol = medium-Fe_2 AND Mg_2
- Img_3 = Img_2 SUBSTRACT (OPX_Ol)
- Plagioclase = Ca_3 AND Al_3
- Img_4 = Img_3 SUBSTRACT Plagioclase
- Silica = Si_4 (only for enclave segmentation)
- (Na,K)Cl = (Na_4 AND Cl_4) OR (K_4 AND Cl_4) (only for enclave segmentation)
- Porosity = BSE (threshold of black areas)
- Analyze particule under ImageJ to calculate the area of each phase. (Na,K)Cl, Silica, Oxides, Apatite <20 pixels in enclaves were excluded. For all other phases, crystals <50 pixels were also removed. This size threshold was applied to ensure the removal of all remnant noises.
- Matrix = 100 - $\sum$ Segmented phases

Minerals with a long axis smaller than 100 μm were counted as matrix phase for techniques (2,3) (except for diktytaxitic enclaves) using ImageJ software, and the proportions of oxides might be underestimated. To ensure the consistency of the dataset, OS30 and OS136 were measured twice with two different methods (1 and 2, 2 and 3, respectively). Errors on point counting have been estimated using (Solomon, 1963) and do not exceed 39% for values over 1 area % (see Table S10 for details). Manual segmentation and chemical mapping yield very similar results (Appendix B). Their errors are assumed much smaller than the point counting one as areas are measured instead of points. For illustration images, QEMSCAN working distance was set to 9–10 mm with accelerating voltage between 10 and 15 keV, a beam current of 10 nA, a dwell time of 10 μs, an aperture of 30 nm and a resolution of 170 dpi.

A.2. Microprobe calibration

CAMECA SX100 calibration standards were wollastonite (Ca, Si), $TiMnO_3$ (Ti, Mn), Al_2O_3 (Al), Cr_2O_3 (Cr), fayalite (Fe), forsterite (Mg), albite (Na, using defocused beam for calibration), orthose (K) and NiO (Ni). The standard deviation of repeat analyses of standard VG-A99 is better than ±5% for all major elements except MnO (± 33.7%) and P_2O_5 (± 17%). CAMECA SXFIVE Tactis calibration standards were San Carlos olivine (Si in olivine), wollastonite (Ca, Si for other silicates minerals), $TiMnO_3$ (Ti, Mn), Al_2O_3 (Al), Cr_2O_3 (Cr), fayalite (Fe), forsterite (Mg), albite (Na), orthose (K) and NiO (Ni). Na-loss in plagioclase using a focussed beam is considered negligible because we used moderate accelerating voltage (15 kV) and current (15 nA) and short counting times (10 s).

A.3. LA-ICP-MS calibration

The following standards were used (Jochum et al., 2005, 2011): [44]Ca for clinopyroxene, plagioclase, amphibole, matrix and [57]Fe for olivine, orthopyroxene, oxides (internal standards), USGS GSD1-G (calibration standard) and NIST 612 plus BCR2-G (secondary standards). Ablation was performed at a frequency of 2 Hz and a fluency of 2.8 J/cm^{2} and conducted in pure He atmosphere. Ablated material was carried to the plasma in an Ar/He/N_2 gas stream. Instrument tuning and mass calibration were performed using NIST 612 (20–40 ppm) reference glass before every analytical session. The standard deviation of repeat analyses of standard BCR2-G is better than ±5% for all trace elements, except for [39]K (27.6%) and [49]Ti (11.3%).

A.4. Bulk compositions

XRF raw data were corrected following the Traill–Lachance algorithm and calibrated using 62 international standards (basalts, syenites, granites,

ultramafic rocks, minerals and soils). Standard list is available in Table S1. Analytical errors on major element chemistry were estimated using repeat analyses of the BEN international standard.

The international standards BHVO-1, SGR-1, JB-3 and GA (Govindaraju, 1994, updated values on GeoReM) and multi-element in-house solutions of 5 and 10 ppb were used for calibration during ICPMS analyses. Analytical errors on trace element chemistry were estimated using repeated analyses of the JB-3 international standard (Govindaraju, 1994, updated values on GeoReM). Accuracy for all major elements is better than 5% except for TiO_2 (5.8%) and P_2O_5 (5.2%) and below 12% for trace elements, except for some elements with low abundance (W up to 37.4%). The 1σ relative error (precision) for all major elements is better than 2% except for MnO (2.2%) and Na_2O (5.5%) and below 10% for trace elements except Ta (16.1%).

In order to get a qualitative assessment of their compositions, the major element bulk composition of diktytaxitic enclaves (<5 mm in size) was calculated using the modal mineral proportions (voids and secondary-phases free) which were obtained from the textural analysis of method (3). The mineral composition was taken from the electron microprobe database. For samples where the enclave's mineral composition was not measured, we used all available host rock mineral compositions to calculate the mean and standard deviation of all possible permutations (Table S11). It resulted in 114,840 permutations (or bulk compositions) for the Hde diktytaxitic enclave, 800 for each Hds and 10,584 for Hdw. The final relative standard deviation (1σ) is better than 10% except MnO (41%) in Hdw, TiO_2 (31%) in Hde, and FeO (11%) and MgO (13%) for Hds1 and Hds2 respectively (Table S11). These large relative errors are due to variability in measured mineral compositions (mostly titanomagnetite variations) and glass compositions.

A.5. Thermobarometry error estimations

The maximum error was deduced by calculating the temperature using the lower bounds of the water content estimates (the lower dashed line in Fig. 10) for both eq. 14 and 34 (Putirka, 2008), the highest bound of the assumed pressure ($P = 2$ kbar for the current pressure assumption) for eq. 34 only, and the final addition of SEE from eqs. 14 and 34, respectively. The minimum error was deduced in a similar way using the maximum water content, minimum pressure ($P = 1$ kbar) minus the SEE from the considered equation. Calculated error for Petrelli et al. (2020) thermometer represents the SEE of the model.

Similarly to temperature, errors calculated for pressure estimates take into account the errors on the calculated temperatures and the SEE of the regression for Neave and Putirka (2017); Putirka (2008) and only the SEE for the two Petrelli et al. (2020) barometers.
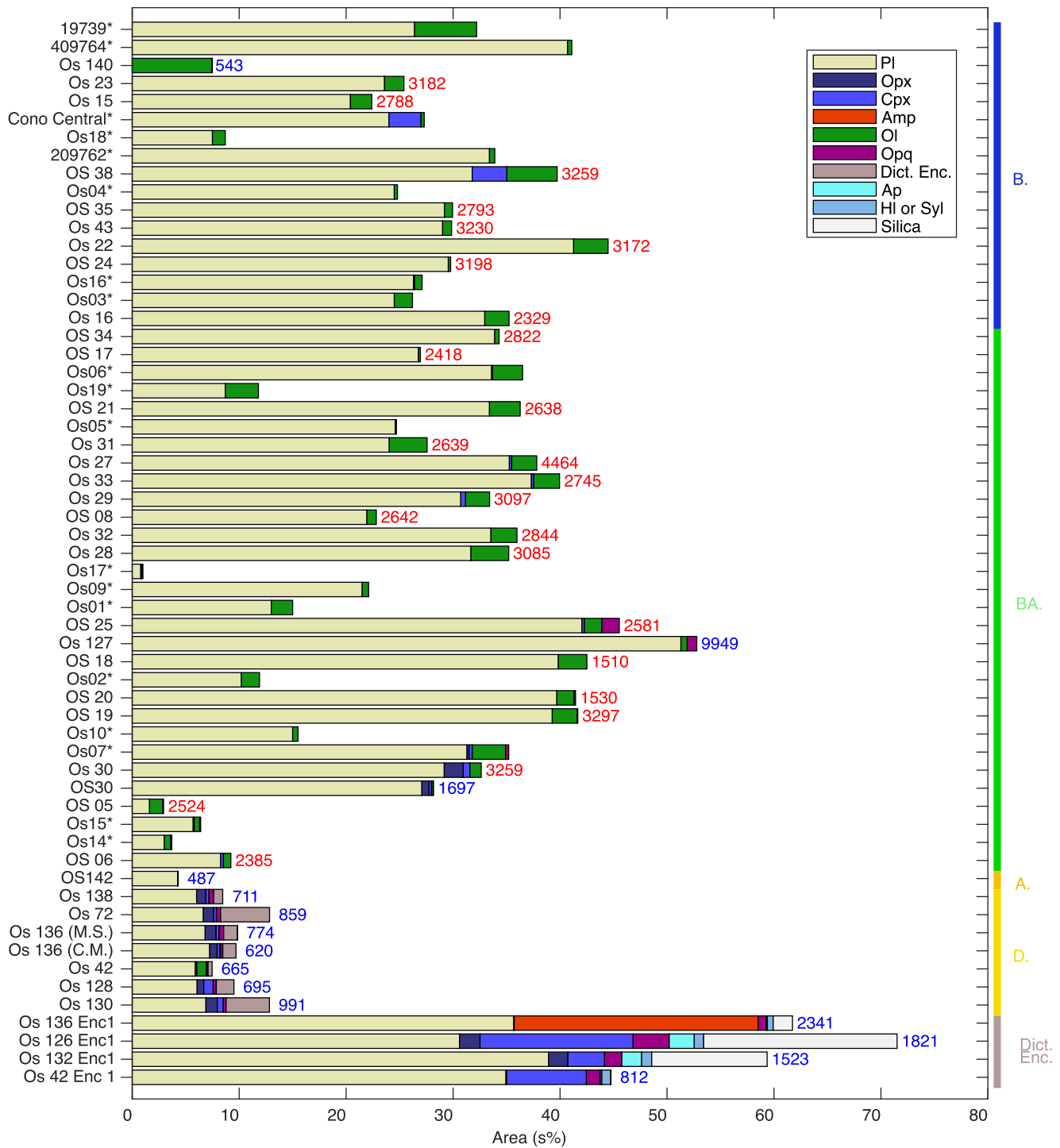
Appendix B. Mineral proportions

Fig. B.16. Area % proportions of the observed mineral phases. Samples names with * are from the literature, red numbers represent the number of points (point counting), the blue ones stand for the number of crystals segmented (manual segmentation or chemical mapping). The samples were sorted using the SiO$_2$ content from the bulk rock (B. = basalt, BA. = basaltic andesite, A. = Andesite, D. = Dacite, Dict. Enc. = diktytaxitic enclaves). (For interpretation of the references to colour in this figure legend, the reader is referred to the web version of this article.)
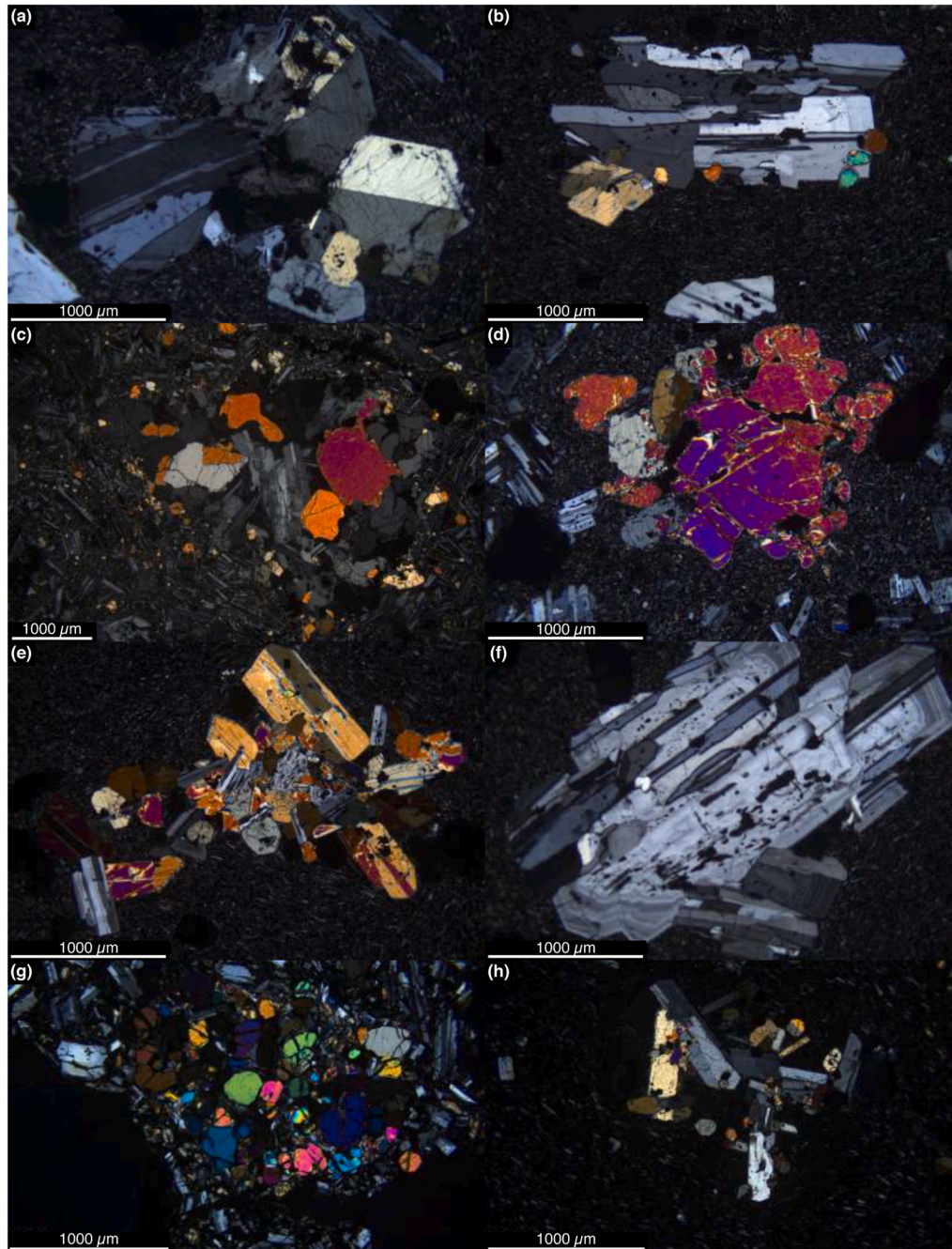
Appendix C. Crystal clots

Fig. C.17. Photomicrographs (crossed polars) of the various types of crystal glomerocrysts (clusters, aggregates, clots. (a) OS6 (evolved basaltic andesite), pyroxenes and plagioclase; (b) OS7 (evolved basaltic andesite), pyroxenes, olivine and plagioclase; (c) OS65 (evolved basalt), olivine and plagioclase; (d) OS27 (primitive basaltic andesite), olivine, clinopyroxene, (plagioclase); (e) OS7 (evolved basaltic andesite), pyroxene, olivine and plagioclase; (f) OS7 (evolved basaltic andesite), plagioclase; (g) OS63 (primitive basaltic andesite), olivine; (h) OS132 (dacite), pyroxene and plagioclase.
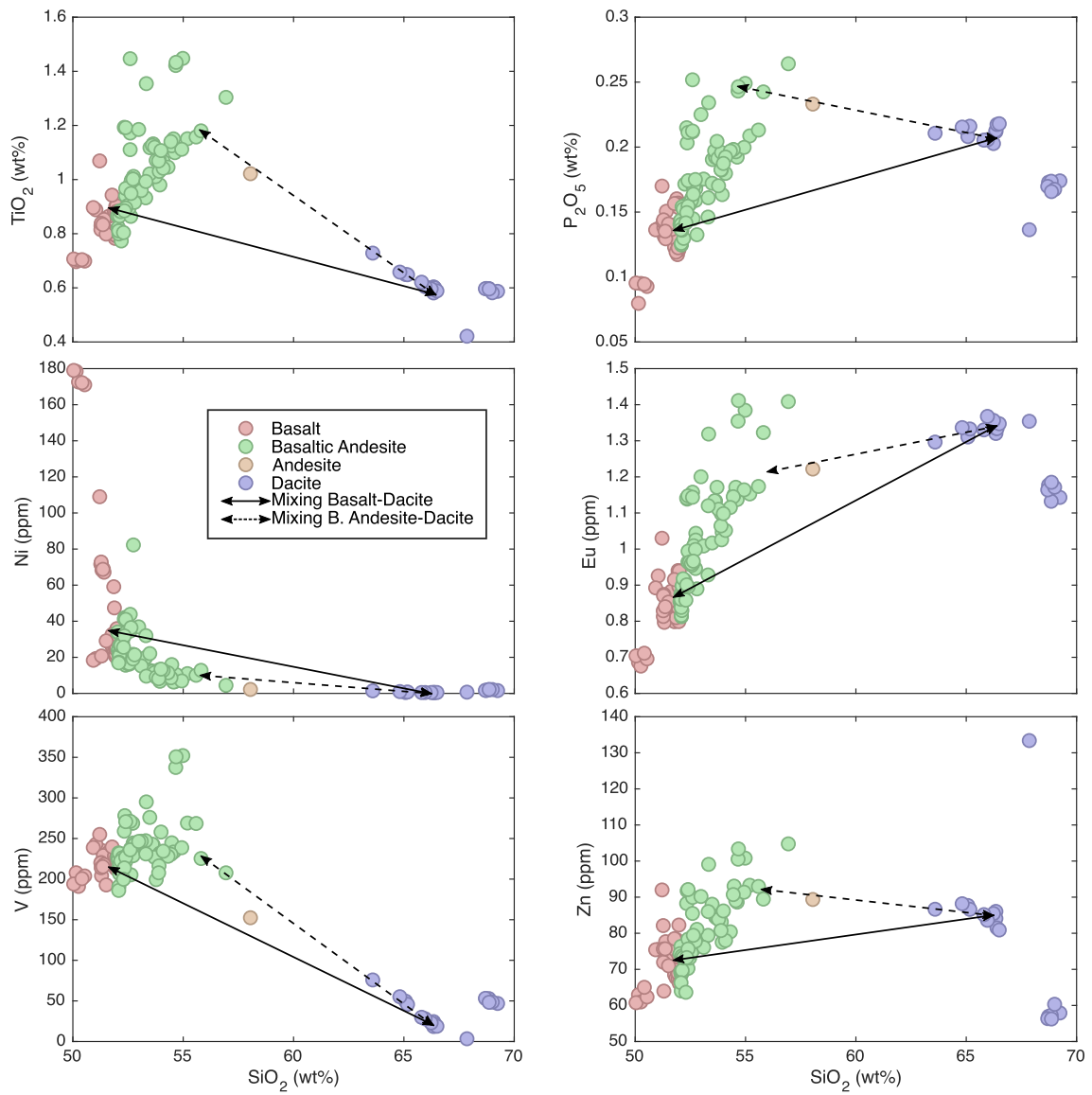
Appendix D. Mixing test

Fig. D.18. Selection of Harker diagrams showing that mixing is not a dominant process at Osorno. In elbow-shaped trends, mixing lines should stand out as straight lines.
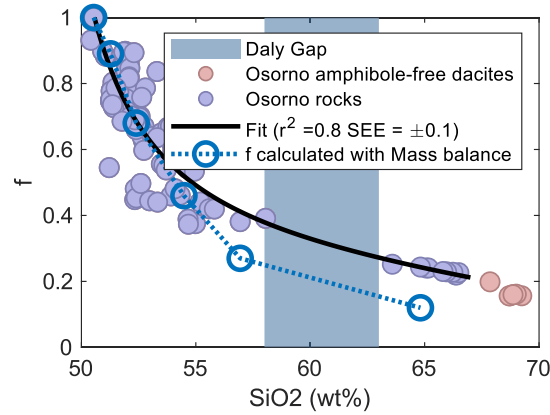
Appendix E. Fractionation rate

Fig. E.19. f values (fractionation rate) estimated using the Rayleigh distillation law and the Zr content of bulk rock compositions. The fit was then used to estimate the H_2O contents using the regression curve.

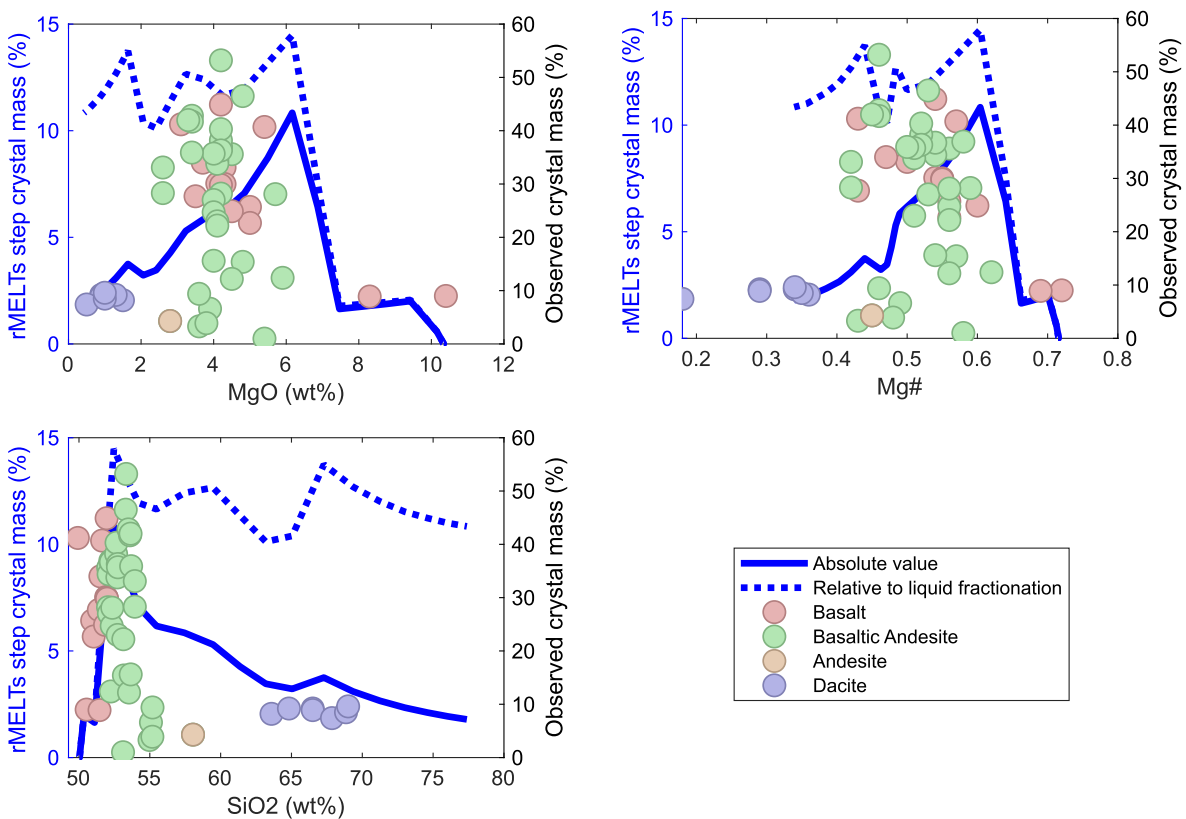## Appendix F. r-MELTs phase proportions

Fig. F.20. Crystal mass from r-MELTs (blue curves, 2 kbar, FMQ, $H_2O = 1$ wt%) and mineral proportions estimations versus different markers of differentiation (SiO_2, MgO, Mg#). The blue curves were drawn considering a perfect fractional crystallization, so the crystal content represents what crystallized at a single temperature step (20°C). We observe that the peak of crystallization in the r-MELTs simulation corresponds to the highest observed crystallinities. All the measured area proportions were assumed to be equal to volume proportions and are expressed in vol%. Values were then converted to wt% assuming the following densities (kg/m³) (Vander Auwera et al., 2021): 3200 (amphibole), 5000 (titanomagnetite), 3200 (orthopyroxene, clinopyroxene), 3300 (olivine), 2700 (plagioclase, matrix). (For interpretation of the references to colour in this figure legend, the reader is referred to the web version of this article.)
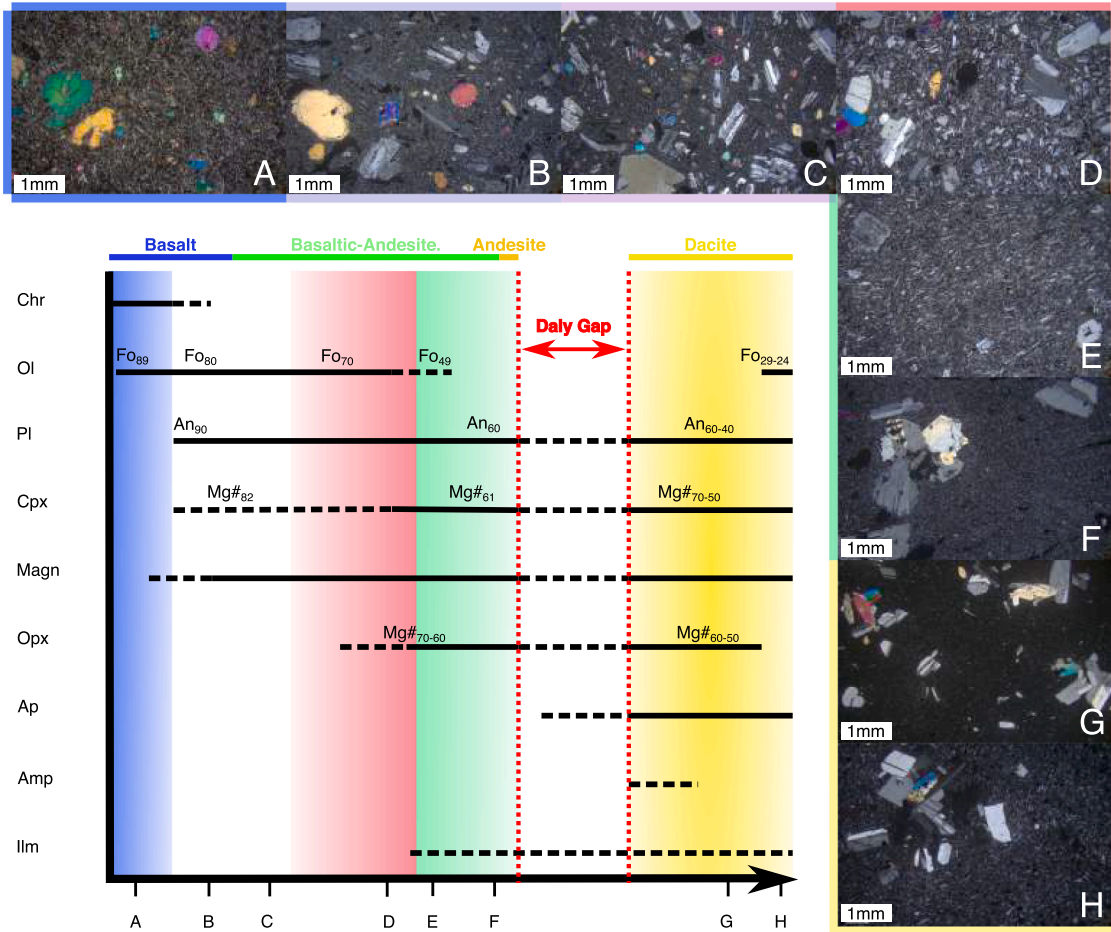
Appendix G. Mineral sequence

Fig. G.21. Relative appearance of the different phases on a differentiation chart (A to H). The microphotographs (crossed polars, same scale) illustrate the evolution of the lava textures with differentiation from a near-primary basalt (A) to a fayalite-bearing dacite (H). Different colors are shown for the dacite (yellow), the primitive basalts (blue), the samples with a very high density of large plagioclase microlith crystals (red) and those with a sharp decrease in the crystallinity and that resemble to the textures of the dacite (green). A = OS82; B=OS109; C=OS38; D=OS20; E = OS142; F=OS06; G = OS130; H OS42. (For interpretation of the references to colour in this figure legend, the reader is referred to the web version of this article.)
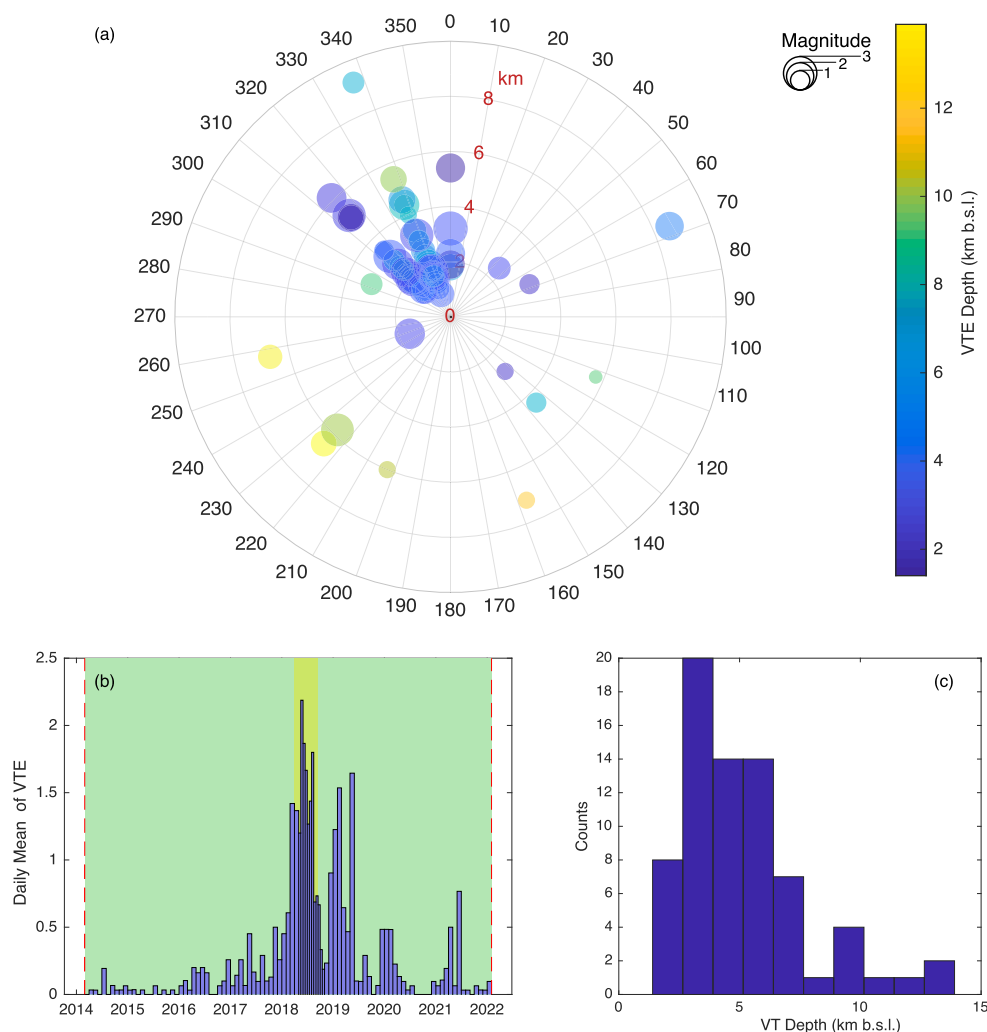
Appendix H. Osorno monitoring

Fig. H.22. (a) Polar plot of the main VT (volcano tectonic events) below Osorno (Ortega, 2021). The origin represents the summit of the volcano. (b) Histogram of the VT daily number mean throughout time. The background colour represents the alert level (green or yellow). (c) Histogram of the main VT depth.

References

Adriasola, A.C., Thomson, S.N., Brix, M.R., Hervé, F., Stöckhert, B., 2006. Postmagmatic cooling and late Cenozoic denudation of the North Patagonian Batholith in the Los Lagos region of Chile, 41° −42° 15′ S. Int. J. Earth Sci. 95, 504–528. https://doi.org/10.1007/s00531-005-0027-9.

Bouvet de Maisonneuve, C., Dungan, M.A., Bachmann, O., Burgisser, A., 2012. Insights into shallow magma storage and crystallization at Volcán Llaima (Andean Southern Volcanic Zone, Chile). J. Volcanol. Geotherm. Res. 211–212, 76–91. https://doi.org/10.1016/j.jvolgeores.2011.09. 010.

Bruhns, W., 1853. Rocas del volcan Osorno. Sociedad nacional de minera, Santiago de Chile, Boletin minero, 254, pp. 338–350.

Castro, J.M., Schipper, C.I., Mueller, S.P., Militzer, A.S., Amigo, A., Parejas, C.S., Jacob, D., 2013. Storage and eruption of near-liquidus rhyolite magma at Cordón Caulle, Chile. Bull. Volcanol. 75, 702. https://doi.org/10.1007/s00445-013-0702-9.

Cembrano, J., Lara, L., 2009. The link between volcanism and tectonics in the southern volcanic zone of the Chilean Andes: a review. Tectonophysics 471, 96–113. https://doi.org/10.1016/j.tecto.2009.02.038.

Contreras Vargas, M.A., Figuerosa Vera, M., Pedreros Delgado, G., 2020. Ranking de riesgo especifico de volcanes activos de chile 2019. URL:https://www.sernageomin.cl/wp-content/uploads/2020/02/Presentaci\%C3\%B3n_Ranking_Volcanes_Sernageomin_2020-web.pdf.

Coombs, M.L., Eichelberger, J.C., Rutherford, M.J., 2002. Experimental and textural constraints on mac enclave formation in volcanic rocks. J. Volcanol. Geotherm. Res. 20.

Costa, F., Scaillet, B., Pichavant, M., 2004. Petrological and experimental constraints on the pre-eruption conditions of holocene dacite from Volcán San Pedro (36°S, Chilean Andes) and the importance of sulphur in silicic subduction-related magmas. J. Petrol. 45, 855–881. https://doi.org/10.1093/petrology/egg114.

Deruelle, B., 1982. Petrology of the plio-quaternary volcanism of the South-Central and Meridional Andes. J. Volcanol. Geotherm. Res. 14, 77–124. https://doi.org/10.1016/0377-0273(82)90044-0.

Díaz, D., Zuñiga, F., Castruccio, A., 2020. The interaction between active crustal faults and volcanism: a case study of the Liquiñe-Ofqui Fault Zone and Osorno volcano, Southern Andes, using magnetotellurics. J. Volcanol. Geotherm. Res. 106806. https://doi.org/10.1016/j.jvolgeores. 2020.106806.

Drignon, M.J., Bechon, T., Arbaret, L., Burgisser, A., Komorowski, J.C., Martel, C., Miller, H., Yaputra, R., 2016. Preexplosive conduit conditions during the 2010 eruption of Merapi volcano (Java, Indonesia). Geophys. Res. Lett. 43 https://doi.org/10.1002/2016GL071153.

Ghiorso, M.S., Gualda, G.A.R., 2015. An H2O-CO2 mixed fluid saturation model compatible with rhyolite-MELTS. Contrib. Mineral. Petrol. 169, 53. https://doi.org/10.1007/s00410-015-1141-8.

Govindaraju, K., 1994. 1994 compilation of working values and sample description for 383 geostandards. Geostand. Newslett. 18, 1–158. https://doi.org/10.1046/j.1365-2494.1998.53202081.x-i1.

Grove, T.L., Donnelly-Nolan, J.M., 1986. The evolution of young silicic lavas at Medicine Lake Volcano, California: implications for the origin of compositional gaps in calc-alkaline series lavas. Contrib. Mineral. Petrol. 92, 281–302. https://doi.org/10.1007/BF00572157.

Gualda, G.A.R., Ghiorso, M.S., Lemons, R.V., Carley, T.L., 2012. Rhyolite-MELTS: a modified calibration of MELTS optimized for silica-rich, fluid-bearing magmatic systems. J. Petrol. 53, 875–890. https://doi.org/10.1093/petrology/egr080.

Hawthorne, F.C., Oberti, R., Harlow, G.E., Maresch, W.V., Martin, R.F., Schumacher, J. C., Welch, M.D., 2012. Nomenclature of the amphibole supergroup. Am. Mineral. 97, 2031–2048. https://doi.org/10.2138/am.2012. 4276.

Hickey-Vargas, R., Sun, M., Holbik, S., 2016a. Geochemistry of basalts from small eruptive centers near Villarrica stratovolcano, Chile: evidence for lithospheric mantle components in continental arc magmas. Geochim. Cosmochim. Acta 185, 358–382. https://doi.org/10.1016/j.gca.2016.03.033.

Hickey-Vargas, R., Holbik, S., Tormey, D., Frey, F.A., Moreno Roa, H., 2016b. Basaltic rocks from the Andean Southern Volcanic Zone: insights from the comparison of along-strike and small-scale geochemical variations and their sources. Lithos 258-259, 115–132. https://doi.org/10.1016/j.lithos.2016.04.014.

Hildreth, W., Moorbath, S., 1988. Crustal contributions to arc magmatism in the Andes of Central Chile. Contrib. Mineral. Petrol. 98, 455–489. https://doi.org/10.1007/BF00372365.

Huber, C., Townsend, M., Degruyter, W., Bachmann, O., 2019. Optimal depth of subvolcanic magma chamber growth controlled by volatiles and crust rheology. Nat. Geosci. 12, 762–768. https://doi.org/10.1038/s41561-019-0415-6.

Irvine, T.N., Baragar, W.R.A., 1971. A guide to the chemical classification of the common volcanic rocks. Can. J. Earth Sci. 8, 523–548. https://doi.org/10.1139/e71-055.

Jackson, M.D., Blundy, J., Sparks, R.S.J., 2018. Chemical differentiation, cold storage and remobilization of magma in the Earth's crust. Nature 564, 405–409. https://doi.org/10.1038/s41586-018-0746-2.

Jacques, G., Hoernle, K., Gill, J., Hauff, F., Wehrmann, H., Garbe-Schönberg, D., van den Bogaard, P., Bindeman, I., Lara, L.E., 2013. Across-arc geochemical variations in the Southern Volcanic Zone, Chile (34.5–38.0˚S): constraints on mantle wedge and slab input compositions. Geochim. Cosmochim. Acta 123, 218–243. https://doi.org/10.1016/j.gca.2013.05.016.

Jacques, G., Hoernle, K., Gill, J., Wehrmann, H., Bindeman, I., Lara, L.E., 2014. Geochemical variations in the Central Southern Volcanic Zone, Chile (38–43˚S): the role of fluids in generating arc magmas. Chem. Geol. 371, 27–45. https://doi.org/10.1016/j.chemgeo.2014.01.015.

Jay, J., Costa, F., Pritchard, M., Lara, L., Singer, B., Herrin, J., 2014. Locating magma reservoirs using InSAR and petrology before and during the 2011–2012 Cordón Caulle silicic eruption. Earth Planet. Sci. Lett. 395, 254–266. https://doi.org/10.1016/j.epsl.2014.03.046.

Jicha, B.R., Singer, B.S., Beard, B.L., Johnson, C.M., Moreno-Roa, H., Naranjo, J.A., 2007. Rapid magma ascent and generation of 230Th excesses in the lower crust at Puyehue–Cordón Caulle, Southern Volcanic Zone, Chile. Earth Planet. Sci. Lett. 255, 229–242. https://doi.org/10.1016/j.epsl. 2006.12.017.

Jochum, K.P., Willbold, M., Raczek, I., Stoll, B., Herwig, K., 2005. Chemical characterisation of the USGS reference glasses GSA-1G, GSC-1G, GSD-1G, GSE-1G, BCR-2G, BHVO-2G and BIR-1G using EPMA, ID-TIMS, ID-ICP-MS and LA-ICP-MS. Geostand. Geoanal. Res. 29, 285–302. https://doi.org/10.1111/j.1751-908X.2005.tb00901.x.

Jochum, K.P., Weis, U., Stoll, B., Kuzmin, D., Yang, Q., Raczek, I., Jacob, D.E., Stracke, A., Birbaum, K., Frick, D.A., Günther, D., Enzweiler, J., 2011. Determination of reference values for NIST SRM 610–617 glasses following ISO guidelines. Geostand. Geoanal. Res. 35, 397–429. https://doi.org/10.1111/j.1751-908X.2011.00120.x.

Klerkx, J., 1964. Etude petrologique de laves des volcans villarica, calbuco, osorno, llaima (chili central). Annales de la Societe Geologique de Belgique 88, 451–469.

Klug, J.D., Singer, B.S., Kita, N.T., Spicuzza, M.J., 2020. Storage and evolution of Laguna del Maule rhyolites: insight from volatile and trace element contents in melt inclusions. J. Geophys. Res. Solid Earth. https://doi.org/10.1029/2020JB019475 n/a, e2020JB019475.

Kress, V.C., Carmichael, I.S.E., 1991. The compressibility of silicate liquids containing Fe2O3 and the effect of composition, temperature, oxygen fugacity and pressure on their redox states. Contrib. Mineral. Petrol. 108, 82–92.

Locock, A.J., 2014. An Excel spreadsheet to classify chemical analyses of amphiboles following the IMA 2012 recommendations. Comput. Geosci. 62, 1–11. https://doi.org/10.1016/j.cageo.2013.09.011.

Lopez-Escobar, L., Parada, M.A., Moreno, H., Frey, F.A., Hickey-Vargas, R.L., 1992. A contribution to the petrogenesis of Osomo and Calbuco volcanoes, Southern Andes (41˚ 00′-41˚ 30′S): comparative study. Andean Geol. 19, 211–226. https://doi.org/10.5027/andgeoV19n2-a05.

Lopez-Escobar, L., Cembrano, J., Moreno, H., 1995. Geochemistry and tectonics of the Chilean Southern Andes basaltic Quaternary volcanism (37-46˚S). Andean Geol. 22, 219–234. https://doi.org/10.5027/andgeoV22n2-a06.

Mandler, B.E., Donnelly-Nolan, J.M., Grove, T.L., 2014. Straddling the tholeiitic/calc-alkaline transition: the effects of modest amounts of water on magmatic differentiation at Newberry Volcano, Oregon. Contrib. Mineral. Petrol. 168, 1066. https://doi.org/10.1007/s00410-014-1066-7.

Marxer, F., Ulmer, P., Müntener, O., 2021. Polybaric fractional crystallisation of arc magmas: an experimental study simulating trans-crustal magmatic systems. Contrib. Mineral. Petrol. 177, 3. https://doi.org/10.1007/s00410-021-01856-8.

McGee, L., Morgado, E., Brahm, R., Parada, M.Á., Vinet, N., Lara, L.E., Flores, A., Turner, M., Handley, H., Nowell, G., 2019. Stratigraphically controlled sampling captures the onset of highly fluid-fluxed melting at San Jorge volcano, Southern Volcanic Zone, Chile. Contrib. Mineral. Petrol. 174, 102. https://doi.org/10.1007/s00410-019-1643-x.

Moreno Roa, H., Naranjo, J.A., Lopez Escobar, L., 1979. Geologia de la cadena volcanica osorno-puntiagudo, andes del sur, latitud 41˚ 10's. In: Paper Presented at the Segundo Congreso Geologico Chileno. Instituto de investigaciones geologicas, Arica, Chile, pp. 109–131.

Moreno Roa, H., Lara, L.E., Orozco, G., 2010. Geologia del volcan Osorno. URL. http://tienda.sernageomin.cl/TiendaVirtual2/ProductDetail.aspx?pid=2290.

Morgado, B.E.E., 2019. Pre-Eruptive Conditions, Crustal Processes, and Magmatic Timescales Recorded in Products of Calbuco and Osorno Volcanoes, Southern Andes. Ph.D. thesis. University of Leeds.

Morgado, E., Parada, M.A., Contreras, C., Castruccio, A., Gutiérrez, F., McGee, L.E., 2015. Contrasting records from mantle to surface of Holocene lavas of two nearby arc volcanic complexes: Caburgua-Huelemolle Small Eruptive Centers and Villarrica Volcano, Southern Chile. J. Volcanol. Geotherm. Res. 306, 1–16. https://doi.org/10.1016/j. jvolgeores.2015.09.023.

Morgado, E., Parada, M.A., Morgan, D.J., Gutiérrez, F., Castruccio, A., Contreras, C., 2017. Transient shallow reservoirs beneath small eruptive centres: constraints from Mg-Fe interdiffusion in olivine. J. Volcanol. Geotherm. Res. 347, 327–336. https://doi.org/10.1016/j. jvolgeores.2017.10.002.

Morgado, E., Morgan, D.J., Harvey, J., Parada, M.Á., Castruccio, A., Brahm, R., Gutiérrez, F., Georgiev, B., Hammond, S.J., 2019b. Localised heating and intensive magmatic conditions prior to the 22–23 April 2015 Calbuco volcano eruption (Southern Chile). Bull. Volcanol. 81, 24. https://doi.org/10.1007/s00445-019-1280-2.

Morgado, E., Morgan, D.J., Castruccio, A., Ebmeier, S.K., Parada, M.Á., Brahm, R., Harvey, J., Gutiérrez, F., Walshaw, R., 2019d. Old magma and a new, intrusive trigger: using diffusion chronometry to understand the rapid-onset Calbuco eruption, April 2015 (Southern Chile). Contrib. Mineral. Petrol. 174, 61. https://doi.org/10.1007/s00410-019-1596-0.

Namur, O., Montalbano, S., Bolle, O., Auwera, J.V., 2020. Petrology of the April 2015 eruption of Calbuco Volcano, Southern Chile. J. Petrol. 61, 33.

Neave, D.A., Putirka, K.D., 2017. A new clinopyroxene-liquid barometer, and implications for magma storage pressures under Icelandic rift zones. Am. Mineral. 102, 777–794. https://doi.org/10.2138/am-2017-5968.

Newman, S., Lowenstern, J.B., 2002. VolatileCalc: a silicate melt–H2O–CO2 solution model written in visual basic for excel. Comput. Geosci. 28, 597–604. https://doi.org/10.1016/S0098-3004(01)00081-4.

Ortega, R., 2021. Reporte Regional de Actividad Volcanica. Technical Report. Servicio Nacional de geologia y mineria. Temuco. From January 2015 to June 2021. Url. https://www.sernageomin.cl/volcan-osorno/.

Panjasawatwong, Y., Danyushevsky, L.V., Crawford, A.J., Harris, K.L., 1995. An experimental study of the effects of melt composition on plagioclase-melt equilibria at 5 and 10 kbar: implications for the origin of magmatic high-an plagioclase. Contrib. Mineral. Petrol. 118, 420–432. https://doi.org/10.1007/s004100050024.

Peccerillo, A., Taylor, S.R., 1976. Geochemistry of eocene calc-alkaline volcanic rocks from the Kastamonu area, Northern Turkey. Contrib. Mineral. Petrol. 58, 63–81. https://doi.org/10.1007/BF00384745.

Petit-Breuilh, M.E., 1999. Cronología Eruptiva Histórica de Los Volcanes Osorno y Calbuco, Andes Del Sur (41o-41o30'S). Technical Report 53. Servicio Nacional de Geología y Minería,. Santiago de Chile.

Petrelli, M., Caricchi, L., Perugini, D., 2020. Machine learning thermo-barometry: application to clinopyroxene-bearing magmas. J. Geophys. Res. Solid Earth 125. https://doi.org/10.1029/2020JB020130 e2020JB020130.

Pichavant, M., Martel, C., Bourdier, J.L., Scaillet, B., 2002. Physical conditions, structure, and dynamics of a zoned magma chamber: Mount Pelée (Martinique, Lesser Antilles Arc). J. Geophys. Res. Solid Earth 107. https://doi.org/10.1029/2001JB000315. ECV 1–1–ECV 1–28.

Plank, T., Kelley, K.A., Zimmer, M.M., Hauri, E.H., Wallace, P.J., 2013. Why do mafic arc magmas contain 4wt% water on average? Earth Planet. Sci. Lett. 364, 168–179. https://doi.org/10.1016/j.epsl.2012.11.044.

Putirka, K.D., 2008. Thermometers and barometers for volcanic systems. Rev. Mineral. Geochem. 69, 61–120. https://doi.org/10.2138/rmg. 2008.69.3.

Ridolfi, F., Renzulli, A., Puerini, M., 2010. Stability and chemical equilibrium of amphibole in calc-alkaline magmas: an overview, new thermobarometric formulations and application to subduction-related volcanoes. Contrib. Mineral. Petrol. 160, 45–66. https://doi.org/10.1007/s00410-009-0465-7.

Ruprecht, P., Bergantz, G.W., Cooper, K.M., Hildreth, W., 2012. The crustal magma storage system of Volcán Quizapu, Chile, and the effects of magma mixing on magma diversity. J. Petrol. 53, 801–840. https://doi.org/10.1093/petrology/egs002.

Ruth, D.C.S., Cottrell, E., Cortés, J.A., Kelley, K.A., Calder, E.S., 2016. From passive degassing to violent strombolian eruption: the case of the 2008 eruption of Llaima Volcano, Chile. J. Petrol. 57, 1833–1864. https://doi.org/10.1093/petrology/egw063.

Rutherford, M.J., Sigurdsson, H., Carey, S., Davis, A., 1985. The May 18, 1980, eruption of Mount St. Helens: 1. Melt composition and experimental phase equilibria. J. Geophys. Res. Solid Earth 90, 2929–2947. https://doi.org/10.1029/JB090iB04p02929.

Ryan, W.B.F., Carbotte, S.M., Coplan, J.O., O'Hara, S., Melkonian, A., Arko, R., Weissel, R.A., Ferrini, V., Goodwillie, A., Nitsche, F., Bonczkowski, J., Zemsky, R., 2009. Global multi-resolution topography synthesis. Geochem. Geophys. Geosyst. 10 https://doi.org/10.1029/2008GC002332.

Schindlbeck, J.C., Freundt, A., Kutterolf, S., 2014. Major changes in the post-glacial evolution of magmatic compositions and pre-eruptive conditions of Llaima Volcano, Andean Southern Volcanic Zone, Chile. Bull. Volcanol. 76, 830. https://doi.org/10.1007/s00445-014-0830-x.

Singer, B.S., Jicha, B.R., Harper, M.A., Naranjo, J.A., Lara, L.E., Moreno-Roa, H., 2008. Eruptive history, geochronology, and magmatic evolution of the Puyehue-Cordón Caulle volcanic complex, ChileEvolution of the Puyehue-Cordón Caulle volcanic complex, Chile. GSA Bull. 120, 599–618. https://doi.org/10.1130/B26276.1.

Sisson, T.W., Grove, T.L., 1993. Experimental investigations of the role of H2O in calc-alkaline differentiation and subduction zone magmatism. Contrib. Mineral. Petrol. 113, 143–166. https://doi.org/10.1007/BF00283225.

Solomon, M., 1963. Counting and sampling errors in modal analysis by point counter. J. Petrol. 4, 367–382. https://doi.org/10.1093/petrology/4.3.367.

Stern, C., Moreno Roa, H., Lopez-Escobar, L., Clavero, J., Lara, L., Naranjo, J., Parada, M., Skewes, A., 2007. Chapter 5. Chilean volcanoes The Geology of Chile. In: Geological Society Special Publication, pp. 147–178. https://doi.org/10.1144/GOCH.

Sun, S.S., McDonough, W.F., 1989. Chemical and isotopic systematics of oceanic basalts: implications for mantle composition and processes. Geol. Soc. Lond., Spec. Publ. 42, 313–345. https://doi.org/10.1144/GSL.SP. 1989.042.01.19.

Tagiri, M., Moreno, H., Lopez-Escobar, L., Notsu, K., 1993. Two magma types of the high-alumina basalt series of osorno volcano, southern andes (41° 06's)-plagioclase dilution effect. J. Mineral. Petrol. Econ. Geol. 88, 359–371. https://doi.org/10.2465/ganko.88.359.

Tassara, A., Echaurren, A., 2012. Anatomy of the Andean subduction zone: three-dimensional density model upgraded and compared against global-scale models. Geophys. J. Int. 189, 161–168. https://doi.org/10.1111/j.1365-246X.2012.05397.x.

Thorpe, R.S., Francis, P.W., O'Callaghan, L., Hutchison, R., Turner, J.S., Moorbath, S.E., Thompson, R.N., Oxburgh, E.R., 1984. Relative roles of source composition, fractional crystallization and crustal contamination in the petrogenesis of Andean volcanic rocks. Philos. Trans. Royal Soc. Lond. Ser. A Math. Phys. Sci. 310, 675–692. https://doi.org/10.1098/rsta.1984.0014.

Tormey, D.R., Frey, F.A., Lopez-Escobar, L., 1995. Geochemistry of the active azufre-planchon-peteroa volcanic complex, Chile (35° 15's): evidence for multiple sources and processes in a cordilleran arc magmatic system. J. Petrol. 36, 265–298. https://doi.org/10.1093/petrology/36.2. 265.

Ulmer, P., Kaegi, R., Müntener, O., 2018. Experimentally derived intermediate to silica-rich arc magmas by fractional and equilibrium crystallization at 1·0 GPa: an evaluation of phase relationships, compositions, liquid lines of descent and oxygen fugacity. J. Petrol. 59, 11–58. https://doi.org/10.1093/petrology/egy017.

Vander Auwera, J., Namur, O., Dutrieux, A., Wilkinson, C.M., Ganerød, M., Coumont, V., Bolle, O., 2019. Mantle melting and magmatic processes under La Picada Stratovolcano (CSVZ, Chile). J. Petrol. 60, 907–944. https://doi.org/10.1093/petrology/egz020.

Vander Auwera, J., Montalbano, S., Namur, O., Bechon, T., Schiano, P., Devidal, J.L., Bolle, O., 2021. The petrology of a hazardous volcano: Calbuco (Central Southern Volcanic Zone, Chile). Contrib. Mineral. Petrol. 176, 46. https://doi.org/10.1007/s00410-021-01803-7.

Waters, L.E., Lange, R.A., 2015. An updated calibration of the plagioclase-liquid hygrometer-thermometer applicable to basalts through rhyolites. Am. Mineral. 100, 2172–2184. https://doi.org/10.2138/am-2015-5232.

Watt, S.F.L., Pyle, D.M., Mather, T.A., Naranjo, J.A., 2013. Arc magma compositions controlled by linked thermal and chemical gradients above the subducting slab. Geophys. Res. Lett. 40, 2550–2556. https://doi.org/10.1002/grl.50513.

Wehrmann, H., Hoernle, K., Garbe-Schönberg, D., Jacques, G., Mahlke, J., Schumann, K., 2014. Insights from trace element geochemistry as to the roles of subduction zone geometry and subduction input on the chemistry of arc magmas. Int. J. Earth Sci. 103, 1929–1944. https://doi.org/10.1007/s00531-013-0917-1.

Weller, D.J., Stern, C.R., 2018. Along-strike variability of primitive magmas (major and volatile elements) inferred from olivine-hosted melt inclusions, southernmost Andean Southern Volcanic Zone, Chile. Lithos 296-299, 233–244. https://doi.org/10.1016/j.lithos.2017.11.009.

Zimmer, M.M., Plank, T., Hauri, E.H., Yogodzinski, G.M., Stelling, P., Larsen, J., Singer, B., Jicha, B., Mandeville, C., Nye, C.J., 2010. The role of water in generating the calc-alkaline trend: new volatile data for Aleutian Magmas and a New Tholeiitic Index. J. Petrol. 51, 2411–2444. https://doi.org/10.1093/petrology/egq062.